Chapter 2
Basics of Voltage Stability Assessment

Amarsagar Reddy Ramapuram Matavalam, Alok Kumar Bharati, and Venkataramana Ajjarapu

2.1 Introduction

From the advent of power generation and induction machines in the 1800s, the power system has been evolving. The power system at large consisted of bulk power generation, transmission system that transported the bulk electrical energy to the load centers, and distribution systems that distributed the bulk energy to individual loads. Power system is probably the biggest machine invented by man. The power grid is a complex interconnected system that spans the geographies of countries and continents. One can trace an electrical path between any two devices connected in the electric grid of these countries or continents. Ensuring the entire grid operates in stable operating conditions under large or small disturbances involves assessment of the operating conditions of the power grid. Since the power system is so large and complex, the power system stability or instability is not a simple classification. Power system instability can occur due to various reasons and can be controlled in various ways. The power system studies used some assumptions like the passive distribution systems: these were pure consumers of electrical energy and that their behavior was well known based on the seasons and the types of loads connected in the system. Until recently, the system had not changed much, and hence the assumptions made about the system and the individual components worked well.

More recently, over the past few decades, with the introduction of distributed generation, increased renewable generation, and fast-changing nature of load is forcing the power system community to reevaluate these assumptions for the various power system studies. In this chapter, we will address the basics of voltage stability

---

A. R. Ramapuram Matavalam · A. K. Bharati · V. Ajjarapu (✉)
Department of Electrical and Computer Engineering, Iowa State University, Ames, IA, USA
e-mail: amar@iastate.edu; alok@iastate.edu; vajjarap@iastate.edu

S. (NDR) Nuthalapati, *Use of Voltage Stability Assessment and Transient Stability Assessment Tools in Grid Operations*, Power Electronics and Power Systems,
https://doi.org/10.1007/978-3-030-67482-3_2

assessment in power systems and some novel methods that are being proposed in the literature that are important under the recently changing distribution systems.

2.1.1 Power System Stability Classification

Stability of a system is a condition of equilibrium between internal and external forces in the system. The ability of the system to return to an equilibrium after a small or large disturbance is often embedded while defining the stability of the system. The stability in power system deals with the various phenomena and components of the power systems that can drive the power system to instability which means drive the system to an operating point from where the system cannot return to its normal operating conditions. The major classification of the power system stability is addressed by the subject matter experts from around the globe that form the IEEE-CIGRE joint task-force has classified the power system stability into ***voltage stability, frequency stability, and rotor angle stability*** [1]. This classification is classical and is continuously evolving with the newer additions of power system components like distributed energy resources (DERs) leading to newer kinds of instabilities manifesting in the power system operations. The definitions and classification were recently updated with the converter/inverter control instabilities that arise from high penetration of DERs or inverter-based resources (IBRs) [2]. The definitions and classification detailed in reference [1] were updated in the IEEE taskforce report on “Stability definitions and characterization of dynamic behavior in systems with high penetration of power electronic interfaced technologies” published in [3].

2.1.2 Voltage Stability

Voltage stability in power systems is the ability of the system to maintain voltages at normal acceptable values at all the nodes in the system at a given operating condition or after a disturbance.

This chapter deals with the fundamentals of voltage stability assessment. This chapter will address some fundamentals of what voltage stability means and how the voltage instability can manifest due to various reasons. Voltage stability assessment in power systems is done differently for long-term and short-term voltage stability. Both, large and small disturbances can result in either short-term or long-term voltage instability in power systems. Voltage instability in a system begins to manifest when there is a continuous drop in voltages or a progressive droop in the bus voltages caused due to a disturbance or increase in the load or a change in operating condition.

We know from fundamental power flow equations that in power systems, the voltage and reactive power are closely related and are coupled. Therefore, the voltage instability problem is usually due to the inability of the system to meet the reactive power demand. Of course, the real power, the network impedances and many other parameters affect the voltage stability of the system, but, fundamentally it is the reactive power demand with losses that are the most crucial when addressing voltage stability problems or voltage instability. The voltage stability of a system is classified into long-term voltage stability and short-term voltage stability. The terms long-term and short-term are defined with respect to the time taken by the system to enter voltage instability after a disturbance or a change in operating point. Further sections address these two kinds of voltage stabilities and the fundamentals of voltage stability assessment for both these kinds of voltage instability.

2.2 Long-Term Voltage Stability

The long-term voltage stability is defined as time scales of a few minutes to few tens of minutes (rarely it can extend to few hours if the voltage instability goes undetected). Voltage collapse is a classic case of long-term voltage instability. The main reason for voltage collapse is the loss of generation or increase in load. The voltage collapse is usually caused due to the saddle-node bifurcation in the system. To understand this phenomenon mathematically, we will look at the basics of the bifurcation theory applied to voltage stability.

2.2.1 Maximum Loading (P-V Curve and Q-V Curve)

Long-term voltage instability or voltage collapse usually occurs due to saddle-node bifurcation. Let us consider a 2-bus system as shown in Fig. 2.1.

The generator terminal voltage and the line reactance is constant. The resistance of the line is assumed to be negligible. The power flow equations for this system can be written as follows:

$$P = \frac{EV}{X}\mathrm{Sin}\,(\theta) \tag{2.1}$$

$$Q = \frac{EV}{X}\mathrm{Cos}\,(\theta) - \frac{V^2}{X} \tag{2.2}$$

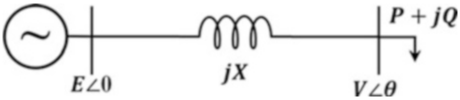

Fig. 2.1 A 2-Bus system with load connected to generator through a transmission line

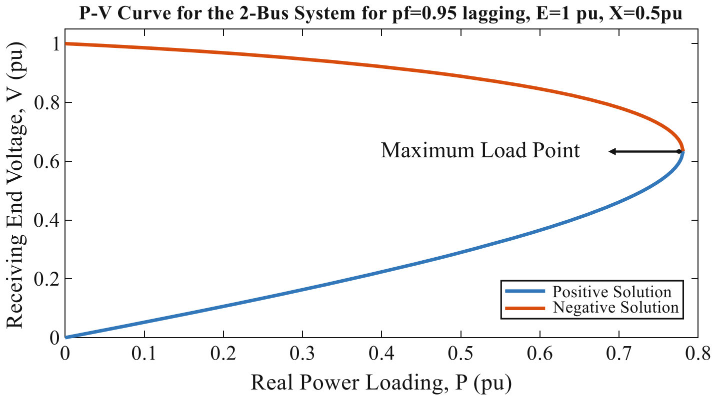

Fig. 2.2 Voltage stability curve ($\lambda - V$ or P-V Curve) for the 2-Bus case

We can write these two equations as functions of the state variables and parameters. The load P, Q can be related with the power factor of the load.

$$\beta = \tan \Phi;\ \text{where, } \phi \text{ is the load power factor angle} \tag{2.3}$$

$$\Rightarrow Q = \beta P \tag{2.4}$$

Using this relation, we square Eqs. (2.1) and (2.2) and simplify to eliminate θ. We get a bi-quadratic equation in V as shown in Eq. (2.5)

$$\left(V^2\right)^2 + \left[2P\beta X - E^2\right]V^2 + P^2X^2\left[1 + \beta^2\right] = 0 \tag{2.5}$$

This can be used to plot the P-V curve, that is using the solution of Eq. (2.6)

$$V = \sqrt{\frac{-\left[2P\beta X - E^2\right] \pm \sqrt{\left[2P\beta X - E^2\right]^2 - 4\left[1 + \beta^2\right]}}{2}} \tag{2.6}$$

By varying P and β we can plot P-V curves. A specific case is shown here for power factor $= 0.95$ lagging, $X = 0.5$ pu and $E = 1$ pu. The positive solution corresponds to the "+" and the negative solution corresponds to the "-" of the "±" in Eq. (2.6). The variation of P and V is shown in Fig. 2.2.

From a given point to the point of saddle-node bifurcation, the power is called the voltage stability margin or the loading limit of the system for the given operating conditions. Researchers have established that voltage instability is mainly caused due to the saddle-node bifurcation in the system [4–9].

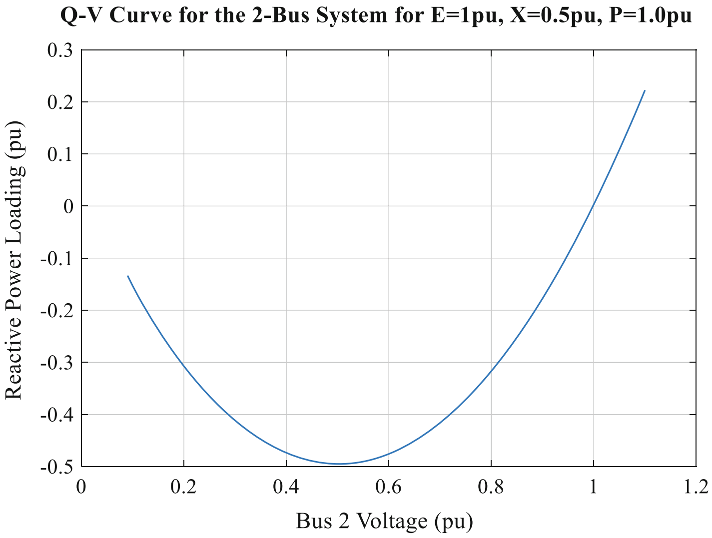

Fig. 2.3 Q-V curve for the 2-Bus case for $P = 0.1$, $E = 1$ pu, $X = 0.5$ pu

Using the solution from Eq. (2.6), for a given P, the angle θ can be calculated from Eq. (2.1) and using that, we can calculate the Q from Eq. (2.2). This results in a Q-V curve shown in Fig. 2.3.

The Q-V curves are typically used for a particular location of interest for locating a synchronous condenser or other reactive power sources. These can be typically drawn with a power flow program. These are typically easier than plotting P-V curves, because in case of P-V curves, at the saddle-node bifurcation point, the power flow solution cannot be solved. The Q-V curve needs one power flow solution and the variation in voltage establishes the amount of reactive power injection required.

2.3 Power Flow Divergence and Instability

The power system is a nonlinear dynamical system. The details of the dynamics and stability are dealt with in great detail by researchers in [4–9]. A bifurcation is an acquisition of a new quality by the motion of a dynamical system, caused by small and smooth changes in its parameters. A power system when undergoes a bifurcation, generally evolves into undesirable states. A saddle-node bifurcation occurs when there is disappearance of an equilibrium caused due to a zero eigenvalue, i.e., an eigenvalue at the origin.

Consider the dynamical power system representations in the mathematical form of differential algebraic equations given by Eq. (2.7)

$$\begin{aligned} \underline{\dot{x}} &= \underline{F}\left(\underline{x}, \underline{y}, \underline{\Lambda}\right) \\ \underline{0} &= \underline{G}\left(\underline{x}, \underline{y}, \underline{\Lambda}\right) \end{aligned} \tag{2.7}$$

In Eq. (2.7),

x represents the state variables of the system like generator rotor angle, speed, dynamic load variables, etc.

y represents the algebraic state variables like voltages and angles at each bus in the system.

λ represents the real and reactive power injections at each bus.

The function F represents the differential equations for the dynamic components in the power systems.

The function G represents the power flow equations and few other algebraic equations in the power system.

The unreduced Jacobian of the system represented by Eq. (2.7) is given as:

$$\underline{J_{DAE}} = \begin{bmatrix} \underline{F}_X & \underline{F}_Y \\ \underline{G}_X & \underline{G}_Y \end{bmatrix} \tag{2.8}$$

$$\begin{bmatrix} \underline{\Delta \dot{x}} \\ 0 \end{bmatrix} = \underline{J_{DAE}} \begin{bmatrix} \underline{\Delta x} \\ \underline{\Delta y} \end{bmatrix} \tag{2.9}$$

Assuming $\underline{G}_Y$ is non-singular, we may reduce Eq. (2.9) by eliminating $\underline{\Delta y}$, which results in the reduced Jacobian matrix and is a Schur's complement. Eq. (2.10) and (2.11) are a result of this elimination of $\underline{\Delta y}$ in the $\underline{\Delta \dot{x}}$ expression:

$$\underline{\Delta \dot{x}} = \left[\underline{F}_X - \underline{F}_Y\, \underline{G}_Y^{-1} \underline{G}_X\right] \underline{\Delta x} \tag{2.10}$$

$$\underline{A} = \left[\underline{F}_X - \underline{F}_Y\, \underline{G}_Y^{-1} G_X\right] \left(\text{Schur}'\text{s Complement}\right) \tag{2.11}$$

From Eq. (2.10) we can clearly see that singularity of $\underline{G}_Y$ causes bad things to happen. Therefore, singularity of $\underline{G}_Y$ is directly associated to instability. The power flow Jacobian J_{LF} is part of $\underline{G}_Y$; $\underline{G}_Y = \begin{bmatrix} D_1 & D_2 \\ D_3 & J_{LF} \end{bmatrix}$. Reference [5] explains under special cases, the $\underline{G}_Y$ is reduced to the power flow Jacobian J_{LF} and singularity of the power flow Jacobian directly indicates the instability of power system.

Section 8 of reference [5] provides a detailed explanation that the singularity of the power flow Jacobian is an indication of the instability of the system. The determination of the point of singularity of the power flow Jacobian is not a trivial problem and continuation methods were applied to determine the point of instability. Development of continuation power flow method helped to determine the point of maximum loading [6].

2.3.1 Continuation Power Flow Applied to Determine Voltage Stability Margin

There are many methods applied for voltage stability margin dependent, and one of the most standard methods is the continuation power flow method.

To understand the continuation method, let us consider the following system equation:

$$g\left(x,\lambda\right)=0 \tag{2.12}$$

In Fig. 2.4, we see if we want to move from solution 1 (x_1,λ_1) to solution 2 (x_2,λ_2), there are multiple ways to accomplish this:

1. We can use a simple straight-line predictor by changing λ to λ_2 and use Newton's method to compute the value of x_2 with x_1 as the initial solution.

$$\begin{aligned} &g_x\left(x^i,\lambda_2\right)\times\Delta x^i=-g\left(x^i,\lambda_2\right)\\ &x^{i+1}=x^i+\Delta x^i \end{aligned} \tag{2.13}$$

Geometrically, this amounts to approximating the curve first by a straight-line predictor and then correcting it at $\lambda=\lambda_2$.

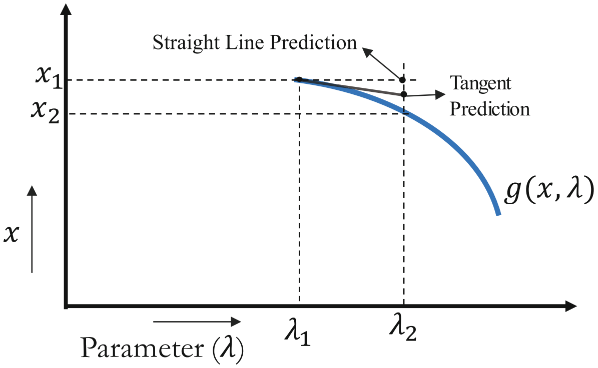

Fig. 2.4 Methods for prediction of the next solution for a change in parameter λ

2. We can use a tangent predictor shown in Fig. 2.4 to arrive at a tangent prediction at $\lambda = \lambda_2$. And then correct it. In this case, as seen, the correction is much smaller than the correction in the straight prediction case.

The continuation power flow method for voltage stability margin assessment uses the second method to determine the maximum load increase parameter $\lambda_{\max}$.

2.4 Parameter Sensitivity in VSM Assessment

The main parameters that affect the voltage stability margin are the nature of load, losses in the system, and generator limits (generator capability). The fundamental purpose of the power system is to ensure there is electrical energy/power delivered to the load. Due to voltage instability, the power transferred to the load becomes limited and at the voltage collapse, the system is unable to supply power to the load. The long-term voltage stability assessment is directly related to the transfer of power from the generator to the load end. The loads in the power system are located at the far end of the distribution feeders and so it is important to account for the distribution system for this analysis. Let us Consider a 2-bus system with a transmission line, a generator, and a load as shown in Fig. 2.5.

We will vary all the parameters to see how they affect the voltage stability margin of this simple extended:

$$R_T + j\ X_T = 0.03 + j\ 0.3 \text{ pu}$$

$$\text{Base Load} = 30 + j\ 10 \text{ MVA}$$

2.4.1 Static Load Models

The nature of load is one of the most important aspects in voltage stability assessment. The load models for long-term voltage stability assessment are mainly static load models like the constant power loads (P), constant current loads (I), and constant impedance loads (Z). There can be combination of these load types as well which are in the form of ZIP loads.

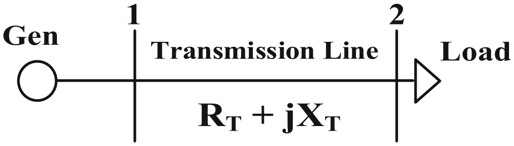

Fig. 2.5 2-Bus system with a load connected to a generator

Equation (2.14) represents the ZIP load models. It can be seen from the ZIP load models that the constant impedance loads are proportional to the square of the voltage fraction, the constant current load is proportional to the voltage fraction, and the constant power is not dependent on the voltage. As the voltage decreases, the constant impedance load reduces maximum and then the constant current load and the constant power does not vary.

$$\begin{aligned} P_{\text{ZIP}} &= P_0\left(P_Z\left(\frac{V}{V_0}\right)^2 + P_I\left(\frac{V}{V_0}\right) + P_P\right) \\ Q_{\text{ZIP}} &= Q_0\left(Q_Z\left(\frac{V}{V_0}\right)^2 + Q_I\left(\frac{V}{V_0}\right) + Q_P\right) \end{aligned} \tag{2.14}$$

Where,

P_0, Q_0→ base real and reactive powers of the load
P_Z, Q_Z →constant impedance fraction of real and reactive power
P_I, Q_I →constant current fractions of real and reactive power
P_P, Q_P →constant power fractions of real and reactive power

$$P_Z + P_I + P_P = Q_Z + Q_I + Q_P = 1$$

$$[\text{ZIP}] = [P_Z \;\; P_I \;\; P_P] = [Q_Z \;\; Q_I \;\; Q_P]$$

Therefore, as the load is increased, the voltage drops, and this has an impact on the voltage-dependent loads in turn. However, for the constant power load, as the line voltage drop increases due to higher load, it results in lower voltage at the load which means the line current increases causing the losses to increase further. Therefore, it is expected that the constant power load results in the lowest voltage stability margin (VSM) keeping all other parameters constant and the highest margin will be for the constant impedance load. Under ideal case, the constant impedance will have an infinite margin. To understand this better, let us consider the system shown in Fig. 2.5. We will model the load as ZIP load and consider three ZIP Profiles: ZIP1 = [0.8 0.1 0.1]; ZIP2 = [0.1 0.8 0.1]; and ZIP3 = [0.1 0.1 0.8]. We will use the continuation power flow to understand the influence of nature of load on VSM. Figure 2.6 shows the P-V curves for the load modeled with different ZIP profiles and the corresponding maximum load increase parameter $\lambda_{\max}$.

2.4.2 *Network Impedance*

The impedance is responsible for the losses in the system and the transfer of power is directly influenced by the losses. Higher losses imply lower capability of transfer of power from the generator to the load. We will vary the transmission line impedance

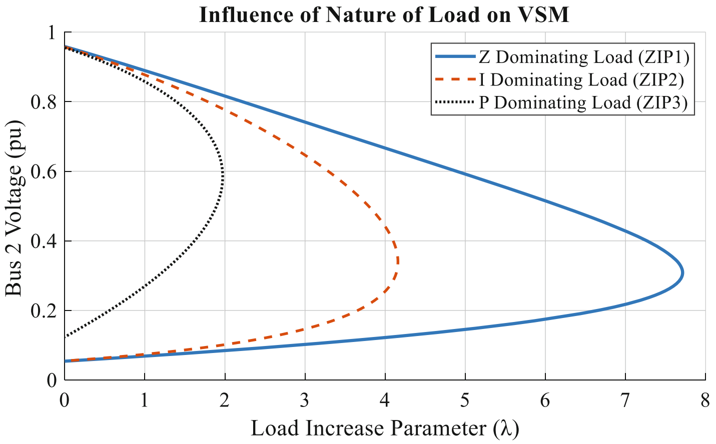

Fig. 2.6 Influence of nature of load on VSM for the extended 2-Bus system

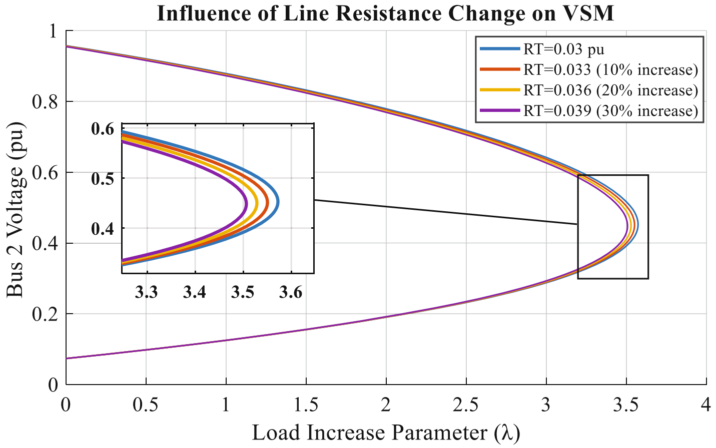

Fig. 2.7 Influence of line resistance on VSM for the extended 2-Bus system

by varying the resistance and reactance separately. And see how they affect the VSM of the system. We will model the load with a ZIP profile of [0.4 0.3 0.3] for all the cases.

We will now see the influence of change in Line reactance on VSM.

From Figs. 2.7 and 2.8, we can see that the change in the line reactance has more influence on the VSM. The reactive power losses are important for voltage stability and since transmission lines usually have low $\frac{R}{X}$ ratios, the real loss impact is lower in the transmission systems compared to the reactive power loss. However, it is important to capture the real and reactive power losses in the systems with significant $\frac{R}{X}$ ratios.

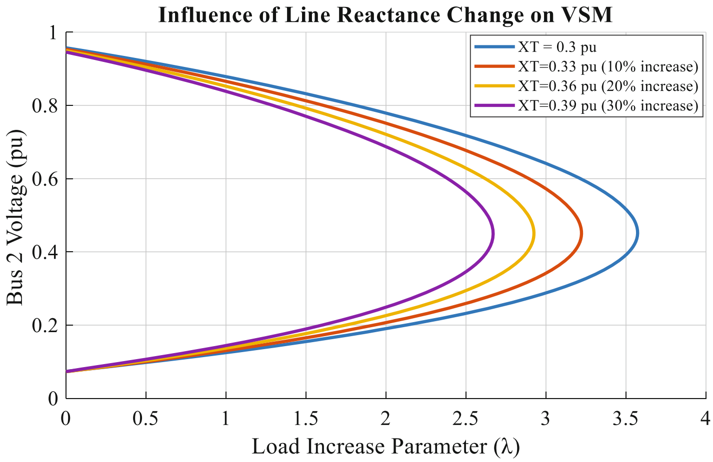

Fig. 2.8 Influence of Line reactance on VSM for the extended 2-Bus system

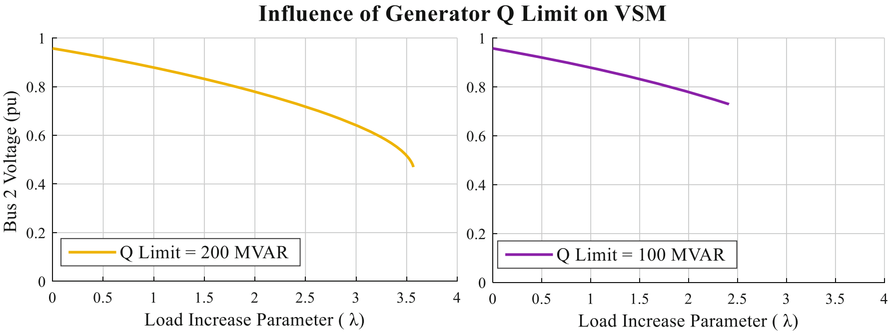

Fig. 2.9 Influence of generator Q_{Limit} on VSM for the extended 2-Bus system

2.4.3 Generator Limits

So far, the reactive power limits of the generator were kept at ±500MVAR. We will modify the reactive power limits of the generator in this section to understand how this influences the VSM assessment. The reactive power limits of the generator directly affect the loading limit as the reactive losses have to be met as the loading increases, the reactive losses increase and if the generator reactive power limit is hit, it is unable to meet the demand of the load any more. The generator reactive power limit is reduced to 200MVAR 100MVAR and the corresponding $\lambda - V$ curves are shown in Fig. 2.9. We can clearly see that the VSM of the system is lower for the case with lesser Q_{limit} in the generator.

2.4.4 *Effect of Transformer Taps on VSM Assessment*

For the simple 2-Bus system shown above, we add a transformer with taps before the load. The transformer secondary is equipped with taps to help restore the voltage in the distribution system as the load increases for the *P*-*V* curve tracing. Figure 2.10 shows the modified system:

For the system shown in Fig. 2.10 the load is increased to draw the *P*-*V* curve for VSM assessment. In this case, the load is modeled as ZIP load with ZIP profile [ZIP] = [0 0 1]. The response of the Tap changer depends on many aspects of the system. A simple case is shown here where the transformer taps are located on the load side and it is similar to an on-load tap changer (OLTC) that helps to restore the voltage on the distribution system side. The taps have a dead-band for voltages and if the voltage is going beyond the dead-band, the taps operate to maintain the voltage within the dead-band.

For this test case, the dead-band of voltages on the load side is 0.9–1.1 pu. The transformers usually have limited taps. In this case as the load is increased, the voltage decreases and since the taps are located on bus 3 and after a certain amount of load increase, the voltage tends to go below 0.9 pu. 0.9 pu is the lower limit of the dead-band, therefore the taps try to restore the voltage back to 0.9 pu by increasing the number of turns. And this is done for further load increase until the maximum number of turns are reached.

Figure 2.11 shows the $P - V$ curves for the cases with tap changer enabled and disabled with the voltages at Bus 2 and Bus 3 for both the cases. The response of the taps is important to be understood in the context of the load models, location for the taps, and location of the controlled bus. The tap positions and the corresponding

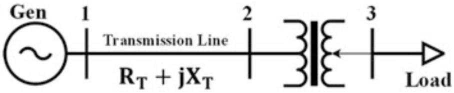

Fig. 2.10 Modified 2-Bus system with taps on the secondary of the substation transformer

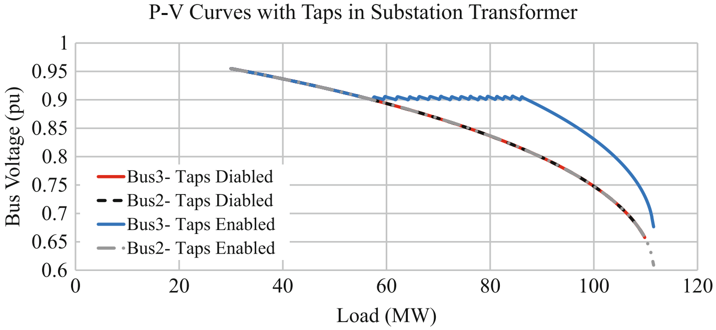

Fig. 2.11 Effect of OLTC tap change on VSM

variations can be captured only through accurate simulation models and correct forms of representing the power flow equations.

As it is seen from Fig. 2.11, even though the taps are enabled, they do not start operating until the voltage has reached the lower limit of the dead-band of the voltage, i.e., 0.9 pu in this case. The taps trying to restore the voltage that enables a higher amount of load increase in the system in this configuration. The taps play an important role in VSM assessment. Reference [8] provides lots of detailed case studies that address the importance of tap changers in VSM assessment.

2.5 Effects of T&D Interactions on Voltage Stability

The recent decades have seen many changes in the way consumers interact with the power grid. The distribution system has seen the integration of various distributed energy resources (DERs). These include electric vehicles, roof-top solar installations, small capacities of distributed wind in the distribution system, battery storage, flexible load, price responsive demand response, etc. as shown in Fig. 2.12.

It is important to understand that modeling distribution system can significantly impact the voltage stability of the system. Traditionally, the distribution systems have been aggregated as a simple load at the load bus in the bulk power system. This is a very drastic method to model the complete distribution system especially for voltage stability studies. Since voltage issues are usually local and require local control, it is important to understand when we model the load and increase the load for voltage stability margin assessment; What does it mean in the real physical world?

The load is located at the terminals of the distribution system feeders. Integration of the DERs in the distribution system has led to situations where there can be two-way power flow in the distribution systems. This is a concern not only for the distribution system operators but also a concern for the transmission system operators as this is largely driven by the renewable uncertainty that causes significant errors in the net-load seen by the transmission system compared to the predicted net-load. This can cause serious issues that are unexpected in the transmission and distribution systems.

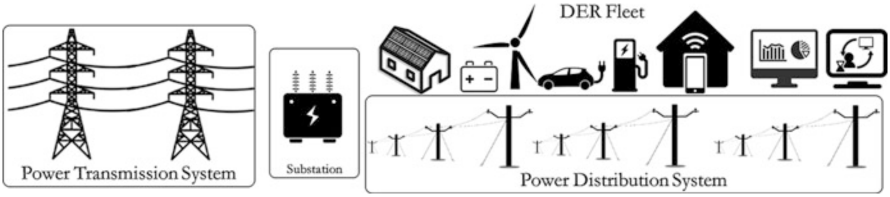

Fig. 2.12 Illustration of various grid-edge technologies (DER Fleet) in the power distribution system

2.5.1 Importance of Modeling Distribution Networks for VSM Assessment

Majority of the DER technologies are integrated into the power system at the distribution level. As discussed earlier, traditionally, the bulk power system studies aggregated the distribution system in the form of a simple constant power load. This is a drastic assumption considering the large number of changes that have occurred in the distribution. North American Reliability Corporation (NERC), a regulating body, also recommends modeling the DERs with as much detail as possible. Lumping the DERs or distributed generation (DG) as negative load is not recommended according to NERC [10]. Federal Energy Regulatory Commission (FERC) has also recently mentioned the need for representing details of the distribution system along with the transmission system for various studies to ensure accurate results and conclusions for planning and operations in power systems [11].

A simple method of modeling the distribution system is to add an equivalent distribution feeder before the load bus at the transmission system. Let us consider extending the 2-bus system with a substation transformer and an equivalent distribution feeder. The equivalent distribution system feeder impedance is calculated based on the IEEE 4-bus distribution system. The load is modeled as a constant power load. The eq. feeder parameters are computed to be $R_D + j X_D = 0.046 + j\,0.095$ pu. The extended 2-bus system is shown in Fig. 2.13. The load is slightly changed according to the load of the IEEE 4-Bus distribution system. The load is modeled as constant power load of $20 + j\,10\,MVA$.

Figure 2.14 shows the CPF results for the cases with and without the equivalent distribution feeder (Eq. D-Feeder) and the impedance added due to the D-Feeder clearly has an impact on the VSM of the system. It is important to model the distribution systems for accurate VSM assessment.

Reference [12] summarizes the different methods of representing distribution system and the respective trade-offs for VSM assessment. The main differences between the transmission and distribution systems are the significant real losses in the distribution systems and three-phase unbalanced operation. Table 2.1 shows the main physiognomies of the distribution system that should be accounted for along with the transmission system models for accurate VSM assessment.

It can be seen from reference [12] that the distribution system unbalance is also an important parameter that needs to be accounted for and for this, three-phase representation is important. The load unbalance effect on VSM is demonstrated below:

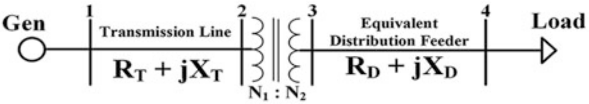

Fig. 2.13 2-Bus equivalent with an equivalent distribution system

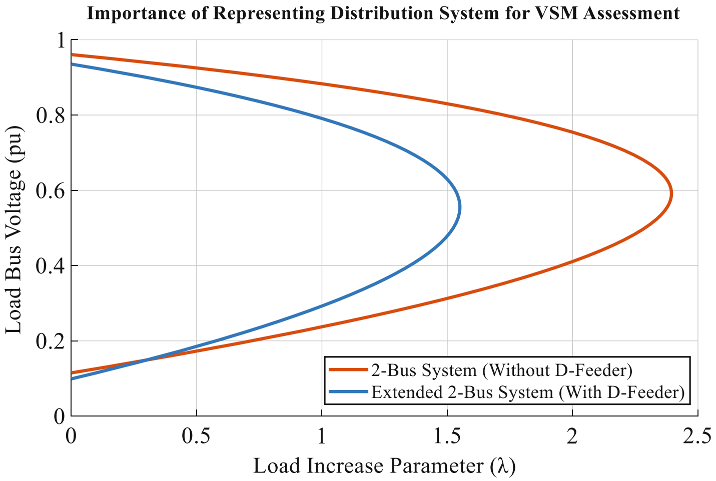

Fig. 2.14 2-Bus equivalent with an equivalent distribution system

Table 2.1 Methods of representing distribution system and the trade-off for VSM assessment [12]

Distribution system Physiognomies ↓	Distribution system physiognomies captured ↓		
	No D-System	Eq. D-Feeder	T&D co-simulation
D-losses	No	Yes (with error)	Yes
D-feeder voltage drop	No	Yes (with error)	Yes
D-feeder segment drop	No	No	Yes
Dist. Unbalance	No	Yes (with error)	Yes
Impact of T on D	No	Yes	Yes

2.5.2 Influence of Load Unbalance on VSM of a System

This is a more recently determined parameter that affects VSM. It directly affects the losses and hence affects the loading limit of the system. To account for the load unbalance in the system, we consider the IEEE 4-Bus distribution system and its losses transferred to the transmission system through the equivalent distribution feeder impedance. Reference [12] provides details of how the unbalance affects the VSM. Like voltage and current unbalance, let net-load unbalance (NLU) be defined as follows:

$$S_{\text{avg}} = \frac{S_A + S_B + S_C}{3} \tag{2.15}$$

$$U_i = \frac{S_i - S_{\text{avg}}}{S_{\text{avg}}} \qquad \forall i = A, B, C \tag{2.16}$$

$$\text{NLU} = \max\left(|U_i|\right) \times 100\% \qquad \forall i = A, B, C \tag{2.17}$$

Table 2.2 Variation of loss as the load unbalance (NLU) increases (same amount of load)

NLU%	Total P loss (W)	P loss/P load (%)	Total Q loss (VAR)	Q loss/Q load (%)
0	419,380	7.77	861,370	32.94
10	428,640	7.94	882,430	33.74
20	460,040	8.52	954,310	36.49
30	514,810	9.53	1,079,410	41.27
40	598,710	11.09	1,270,430	48.58
50	729,460	13.51	1,567,110	59.92
55	830,870	15.39	1,796,630	68.70
60	1,016,220	18.819	2,215,500	84.71

Where,

S_A, S_B, $S_C \rightarrow$ The net-loads on phases A, B, C.

NLU % → Percentage of maximum net-load unbalance.

The Loss is computed for the standard IEEE 4-Bus system with constant power loads for various load unbalance levels and the results demonstrate how the losses increase with increase in load unbalance. The increase in loss is further extended to show the increase in the effective impedance of the equivalent distribution feeder and thereby its effect on the VSM of the system. The load on the system is modeled as constant power loads to ensure the variation in losses observed is due to the load unbalance and no other parameters influence the increase in the losses.

The load is varied by varying the load on phase 'A' and 'C' to create an unbalance in the IEEE 4-Bus distribution system. Care is taken to ensure the total three-phase load is kept the same. The power factor of the load is also kept same ensuring the reactive power is also constant and the unbalance in the real and reactive powers are the same. Table 2.2 shows the results of the IEEE 4-Bus system loss for various percentages of NLU. We can see that the real and reactive losses increase with the load unbalance. The loss is expressed as percentage of load also and it can be seen for higher NLU, loss percentage is much higher than that for a lower NLU%. It can also be seen that the reactive loss % for a higher NLU are much higher than the real power losses and this is very important as this has a significant impact on the overall voltage stability margin of the system and this can be effectively captured by representing the distribution system in detail.

The Eq. D-Feeder parameters, $R_D + jX_D$, are calculated for the IEEE 4-bus system for various NLU. The results from Table 2.2 are used for determining the corresponding Eq. Feeder Parameters of the eq. distribution system. For each of the NLU case, the Eq. D-Feeder parameters are computed in pu for the IEEE 4-Bus system and are shown in Table 2.3.

We performed the continuation power flow on the extended 2-bus system for the various NLU cases and the results are shown in Fig. 2.15 for some of the cases. The results in Fig. 2.15 shows that the effect of increased eq. D-Feeder impedance is the reduction in margin. In addition, as the unbalance increases the amount of reduction in VSM increases further.

Table 2.3 Eq. D-Feeder parameters for the extended 2-Bus system

NLU%	Real loss (kW)	Reactive loss (kVAR)	$R_D + X_{Di}$
0	419.4	861.4	0.0463 + 0.0951i
10	428.6	882.4	0.0473 + 0.0974i
20	460.0	954.3	0.0508 + 0.1053i
30	514.8	1079.4	0.0568 + 0.1191i
40	598.7	1270.4	0.0661 + 0.1402i
50	729.5	1567.7	0.0805 + 0.1729i
55	830.9	1796.6	0.0917 + 0.1983i
60	1016.2	2215.5	0.1121 + 0.2445i

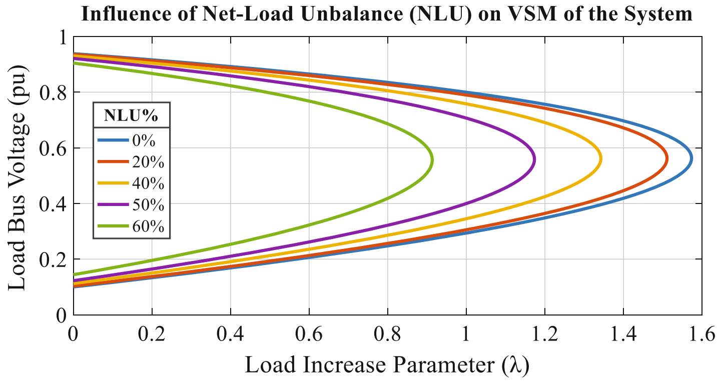

Fig. 2.15 Voltage stability curves for the extended 2-Bus system for various NLU% [12]

The three-phase continuation power flow discussed in [13–14] also demonstrates this for larger transmission system cases where the complete system is modeled in three phases. Much of this unbalance in real life is creeping in from the distribution systems. The distribution system operation is varying fast with the introduction of various grid-edge technologies. The load unbalance coupled with the integration of various distributed generation (DG) or distributed energy resources (DERs) can interact in ways that the net-load unbalance can be significantly high to affect the voltage stability of the system.

Table 2.1 shows that T&D co-simulation is an effective tool to capture both the transmission and distribution system physiognomies for voltage stability assessment and we briefly introduce some preliminary results of using T&D co-simulation for VSM assessment. Reference [12] provides details of the importance of modeling distribution system along with the transmission system for VSM assessment.

2.5.3 T&D Co-Simulation and its Application for VSM Assessment

T&D Co-simulation based on the method of solving coupled systems in a decoupled way. Researchers have been experimenting with different methods of performing T&D co-simulation and some are more practical and seamless than the others. The most commonly used method for T&D co-simulation is based on Master-Slave Splitting where the distribution system substation is the point of coupling between the T&D systems and convergence of solutions from both, the T-System and the D-System is measured based on the Substation voltages and powers. The assumption is that at the substation the voltages are balanced and the unbalance in the distribution is not transferred to the transmission side due to the use of load balancing equipment and reduction in unbalance due to the aggregated effect of the multiple distribution system feeders. Ideally, the unbalance effects are seen in the parts of sub-transmission systems as well. Identification of the boundary bus for T&D co-simulation is very important as also stated in Reference [12].

2.5.3.1 T&D Co-Simulation Framework for Steady-State and Quasi-Steady-State Studies

T&D co-simulation enables detailed modeling of both: the transmission and the distribution systems. This method of simulating the power systems captures all the details of the distribution system along with the inter-dependent nature of the transmission and the distribution systems. The trade-off however is the computational complexity and burden is increased leading to a longer time of simulation. T&D co-simulation employed in large systems requires to use commercial grade solvers for the transmission and distribution systems. The co-simulation method does not require development of new transmission system solvers or distribution system solvers, but, it efficiently integrates existing solvers that can be scaled to large systems in an easy way.

The methodology leveraged for T&D co-simulation is the "Master-Slave" method described by the authors of [15] and [16]. The master-slave method for transmission and distribution (T&D) system co-simulation considers the transmission network as the "Master" and the distribution networks as the "Slave" systems, respectively. Reference [15] is a textbook that discusses the detailed mathematical fundamentals necessary to establish the distributed method of solving coupled problems. Reference [15] discusses various implications of optimizations, dynamic co-simulation, and steady-state co-simulation formulations and the numerical stability of a T&D co-simulation framework that works on "Master-Slave Splitting" (MSS) method. A simple representation of T&D co-simulation framework is shown in Fig. 2.16.

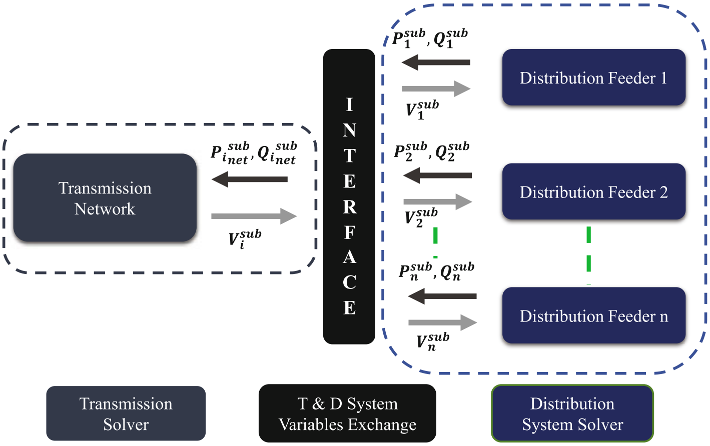

Fig. 2.16 Transmission and distribution co-simulation framework

Reference [12] provides an interface written in python to co-simulate opensource transmission and distribution solvers like Pypower and GridLAB-D. The interface code is written in python and is responsible for exchanging the variables between the transmission and distribution systems. The interface execution does not need any additional software and has built-in features for plotting and can be extended to generate reports as well. Effective T&D co-simulation tightly couples the T&D systems while performing the co-simulation, i.e., the transmission and distribution systems solutions are solved till the substation voltage reaches convergence for a given operating point. The T&D co-simulation framework is also extended to co-simulate commercial solvers on the transmission systems as many of the utilities use the commercial software for their system studies. Reference [12] mentions the use of co-simulating PSSE and GridLAB-D for T&D co-simulation. The salient features of the developed co-simulation interface to co-simulate PSSE and GridLAB-D for steady-state and quasi-steady-state simulations are:

1. The interface is developed using Python which is opensource and provides a simple way to operate GridLAB-D or OpenDSS which are also opensource.
2. The interface is parallel computing compatible and can interface multiple load buses to different distribution systems.
3. The interface can seamlessly integrate with other solvers as well but might need small tweaking to ensure its functionality with the solver. The solver is python version independent.
4. The interface developed can be effectively used for plotting and post simulation report generation.

2.5.3.2 T&D Co-Simulation Tool for Long-Term Voltage Stability Margin Assessment

The T&D co-simulation tool can be effectively used for VSM assessment using the method of identifying the loading limit by means of power flow divergence by slowly increasing the load in the system. Figure 2.17 shows the flowchart for the application of the T&D co-simulation for VSM assessment. The P-V curve tracing method is used for determining the loading limit on the system. The load increase direction is clear in this method as the load increase is not aggregated but each individual load in the distribution system is individually increased. For each loading point or operating point on the *P*-*V* curve, the transmission and distribution systems are co-simulated until the substation voltage converges, and this operating point is recorded to be plotted on the *P*-*V* curve. After the operating point is recorded, the load is slightly increased further by a small step and T&D co-simulation is carried out. This is continued till either system reaches its loading limit, i.e., the power flow diverges.

Figure 2.18 provides the preliminary results on a simple test system where the IEEE 9-Bus transmission system is co-simulated without distribution system representation, with eq. feeder and T&D co-simulation for balanced and unbalanced load as per the IEEE 4-Bus feeder datasheet.

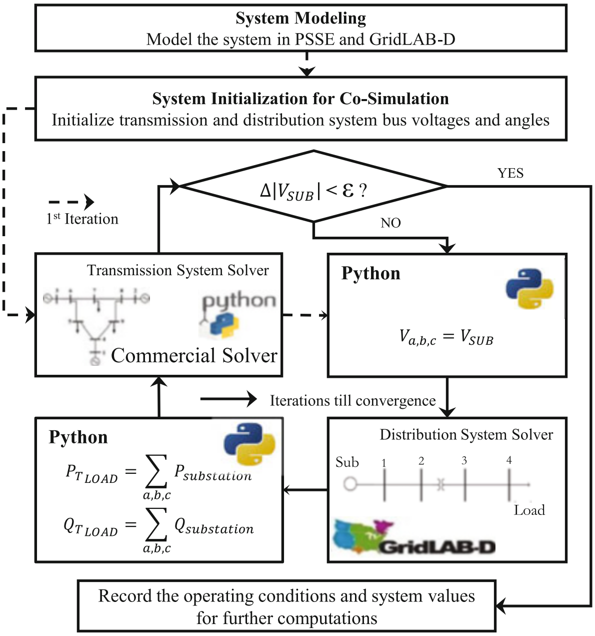

Fig. 2.17 Flow chart for one operating point on *P*-*V* curve to determine VSM [12]

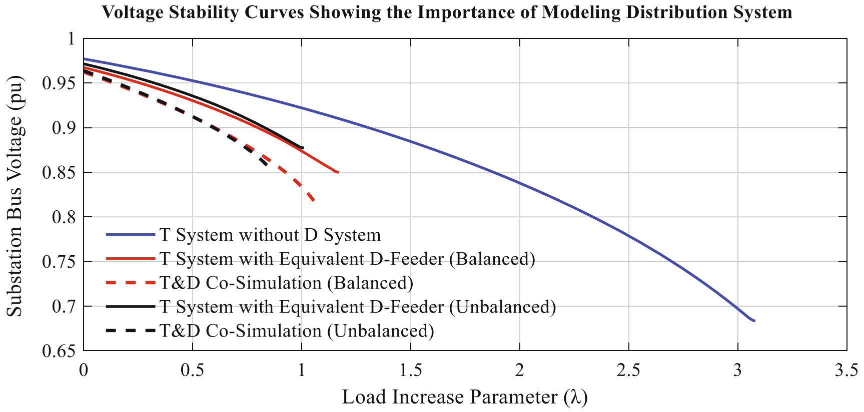

Fig. 2.18 Voltage stability curves with various method of simulations: IEEE 9-Bus transmission + IEEE 4-Node distribution system [12]

Figure 2.18 shows voltage stability curves corresponding different forms of representing the distribution system along with the transmission system for the voltage stability margin assessment. The blue curve is for the case with the transmission system where the distribution system losses are modeled as a part of the load and no distribution system network is represented (The loss is not modeled accurately in the lumped load + loss model). As discussed earlier, the distribution system can be represented as an equivalent feeder as it captures the distribution system physiognomies to a reasonable extent if there is not much unbalance in the system. For the equivalent distribution system feeder (D-Feeder) representation, the D-Feeder parameters are computed for balanced and unbalanced IEEE 4-Bus distribution system. The voltage stability curves for the balanced and unbalanced cases with equivalent feeder method are shown by the red and black curves, respectively. As described in Table 2.1, T&D co-simulation is an effective method to capture the distribution system physiognomies. The voltage stability curves with the T&D co-simulation method with the balanced and unbalanced IEEE 4-Bus distribution system are shown by the red and black dotted curves, respectively. The difference between $\lambda_{\max}$ for the balanced case is not much for the balanced case but for the unbalanced case, there is a significant error. Therefore, for unbalanced distribution systems, using T&D co-simulation is an effective method for VSM assessment.

2.5.3.3 Influence of DER on VSM

The distribution system is changing fast with the integration of various kinds of distributed energy resources (DERs) or distributed generation (DG). The DG when added in the distribution system can aggravate the unbalance in the distribution system if they are not added in a planned manner to ensure there is not high amounts of net-load unbalance. To study this further a simple case study is systematized. In this case study, DG in the form of solar PV inverters are added in the distribution system. The DG is added in different proportions, some extreme three-phase distribution of DG is chosen for 60% of DG added in the distribution system. The system considered is the IEEE 9-bus and IEEE 4-bus distribution system for T&D co-simulation. The DG added in the system is operating in two operating modes: unity power factor (UPF) and volt-VAR control (VVC) mode. The load is modeled with a ZIP profile $[ZIP] = [0.4\ 0.3\ 0.3]$. The distribution system load is unbalanced with the load distribution as: $A = 28.05$ MW; $B = 39.6$ MW; and $C = 52.25$ MW seen at the transmission system load bus. The total MW of DG added =71.94 MW (60% of total load).

The distribution of this ~72 MW of DG is different in the different phases in the three-phase system. In one case the DG is distributed in equal proportion of load, i.e., 60% of load on each phase, and, in other cases, there is low DG penetration in one of the phases and the other two phase % is adjusted to have the total DG added in the system to be ~72 MW. The DG penetration is computed with respect to load in that phase. For example, DG penetration in A-phase- %A = 10% means, amount of DG is 10% of phase-A load.

The *P*-*V* curves for all the cases of DG are shown in Fig. 2.19 which shows that for the same amount of DG added in different proportions, the VSM of the system can be different. This is primarily caused by different amount of NLU in the system, in turn resulting in different amounts of losses. Figure 2.19 also shows that for each case, the VSM for DG in VVC mode is higher than the VSM of DG in UPF mode because in the VVC mode, the smart inverter supplied additional reactive power to maintain the voltage set-point of the inverter. The additional reactive power helps to allow for a further load increase resulting in a larger VSM.

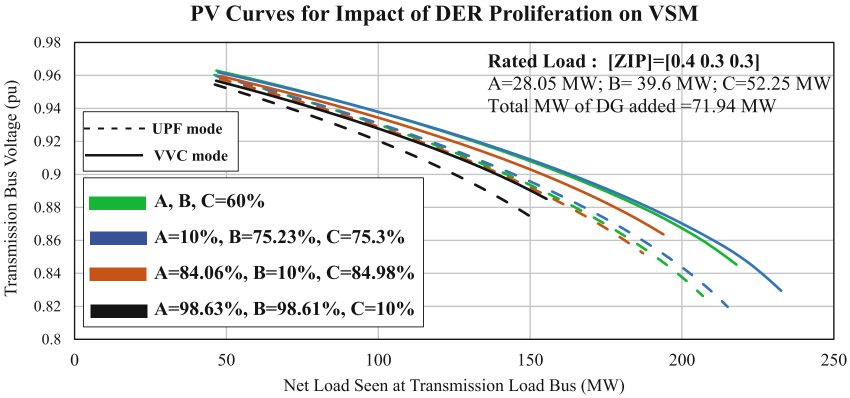

Fig. 2.19 Voltage stability curves for DG proliferation in various proportions—IEEE 9-bus transmission and IEEE 4-bus distribution systems [12]

DG helps increasing the margin but, to determine by how much, depends on how the DG proliferation occurs in the system with respect to the three phases. With the recent amendments to the IEEE 1547 standard, it is important to understand the impact of volt-var control (VVC) on the VSM and the influence of DG distribution on VSM compared to UPF.

2.6 Data-Driven Methods for Long-Term Voltage Stability Assessment

There have been recent efforts done to utilize the online measurements to estimate the margin or an index that can be used as a proxy for the long-term voltage stability. They can be split into methods requiring local measurements and centralized measurements. As the Thevenin methods are of interest in this dissertation, they are discussed in more detail. The main idea behind the Thevenin methods is to estimate an equivalent circuit for the system at the critical load and utilize the ratio between the load impedance and Thevenin impedance as an indicator of long-term voltage stability.

2.6.1 Local Thevenin Equivalent-Based Methods

The early Thevenin methods used only local PMU measurements and independently calculated the Voltage Stability Index (VSI) at each monitoring bus [17, 18]. The VSI was either used to initiate local control actions or transmitted to a centralized location for visualization or control applications. These techniques exploit the high sampling rate of the PMUs (30 samples per second) to capture small variations in the bus voltage at a quasi-steady state operating point and calculate a Thevenin equivalent circuit at each monitored bus. The estimated Thevenin equivalent parameters are then used to calculate the VSI at a bus. To improve accuracy, a multi-bus equivalent is proposed for load areas with several tie-lines [10] and an analytical derivation of the maximum power is used to monitor voltage stability.

One drawback of the local approaches is the reliance on the quasi-steady-state nature of the system. The small variations could be due to a specific phenomenon (forced oscillations, etc.) that skew the measurements and provide a false equivalent. Furthermore, measurement noise in the PMU can cause the LTI to oscillate wildly. This is a well-documented problem and [18] use multiple measurements over a time window to smooth out the errors by mathematical techniques. However, these methods assume a certain noise profile and might not work in presence of certain system behavior. Despite these drawbacks, the simplicity and local nature of these methods make them attractive to utilities and they have been implemented commercially in the field and can trigger emergency corrective actions [20].

2.6.2 Centralized Thevenin Equivalent-Based Methods

The centralized Thevenin methods are calculated at the EMS where the state estimation results and PMU measurements are available for the entire system. Since these methods do not utilize any quasi-steady-state nature of the system for the Thevenin equivalent calculation, they are more robust to noise compared to the local methods. However, the centralized nature means that these methods cannot be used for corrective schemes and instead are best used for preventive schemes. The initial method utilized a simplifying assumption to define the L-index [21], without explicitly calculating a Thevenin equivalent. This idea was formalized by the concept of coupled single-port circuit model [22] which is used to explicitly define a Thevenin equivalent. By utilizing the network equations relating the voltages and currents, the entire system can be equivalently described by an extended Thevenin circuit which includes an extra component (source, load, or impedance) to reflect the coupling with current injections at other load buses and generators. The more recent methods have included the reactive limits into the method by fitting a cubic curve and estimating the generators reaching the limit [23]. [24] presents a method to estimate the maximum power transfer in a transmission corridor utilizing the line admittances. A different paradigm by using the system Jacobian along with the admittance matrix to calculate the Thevenin impedance is proposed in [25]. In the next section, we demonstrate how the sensitivities calculated from the Jacobian are related to the Thevenin Index [26].

2.6.3 Sensitivity-Based Thevenin Index

Fig. 2.20 shows the 2-bus equivalent at a load bus where the rest of the system is reduced into an equivalent voltage $\boldsymbol{E_{th}}$ and an equivalent impedance $\boldsymbol{Z_{th}}$. At low loading, $|\boldsymbol{Z_L}| > |\boldsymbol{Z_{th}}|$ and at critical loading, $|\boldsymbol{Z_L}| = |\boldsymbol{Z_{th}}|$. Thus, the ratio between $|\boldsymbol{Z_L}|$ & $|\boldsymbol{Z_{th}}|$ can be used as an indication of voltage stability and is referred to as Local Thevenin index (LTI) [17, 18] as shown in (2.20).

In principle, two subsequent phasor measurements of the pair $\boldsymbol{V}$ & $\boldsymbol{I}$ can be used to compute $\mathbf{Z_{th}}$ under the assumption that the equivalent parameters do not change

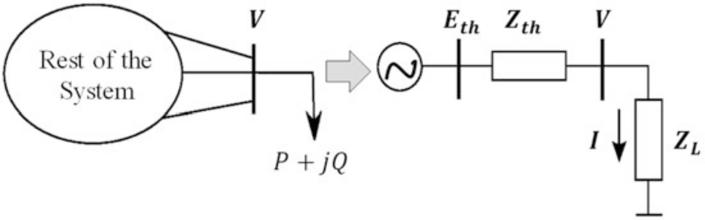

Fig. 2.20 The reduction of the rest-of-the-system into an equivalent $\mathbf{Z_{th}}$ and $\mathbf{E_{th}}$

during the time interval between the two subsequent measurements [17]. This assumption is valid when the load increment (Δλ) between the two measurements is as close to 0 as possible. In practice, Δλ between subsequent measurements is very small (~0.1%) and thus we can use this assumption but theoretically, the ideal value of the $\mathbf{Z_{th}}$ is determined when the load increment is as close to 0 as possible (i.e., $\Delta\lambda \rightarrow 0$). The conventional Local Thevenin index (LTI) at a load Bus *i*, uses the Thevenin Impedance and the Load Impedance and can be determined by Eq. (2.18), using two distinct operating points [17].

$$Z_{th_i} = -\frac{V_i^{(2)} - V_i^{(1)}}{I_i^{(2)} - I_i^{(1)}} = -\frac{\boldsymbol{\Delta} V_i}{\boldsymbol{\Delta} I_i} \tag{2.18}$$

$$Z_{L_i} = \left(\frac{V_i^{(1)}}{I_i^{(1)}}\right) \tag{2.19}$$

$$\mathrm{LTI}_i = \left|\frac{\boldsymbol{Z_{th}}}{\boldsymbol{Z_L}}\right| = \left|\frac{\boldsymbol{\Delta V_i}}{\boldsymbol{V_i^{(1)}}}\right| \cdot \left|\frac{\boldsymbol{I_i^{(1)}}}{\boldsymbol{\Delta I_i}}\right| \tag{2.20}$$

The closer the operating points are, the better the estimate of the Thevenin impedance and the accuracy of the LTI. For simplicity, the loading direction is assumed to be proportional to the initial load implying that the Δλ at all the buses is same. Let the load voltage at the first instance be $(V)e^{j(\theta)}$ and at the second instance can be expressed as $(V + \Delta V)e^{j(\theta + \Delta\theta)}$. As the LTI depends on the Δλ chosen, it is explicitly written as a function of Δλ, using the expression LTI(Δλ) [26].

$$\mathrm{LTI}\,(\Delta\lambda) = \left|\frac{\boldsymbol{Z_{th}}}{\boldsymbol{Z_L}}\right| = \sqrt{\frac{\left(\frac{\Delta V}{\Delta\lambda}\cdot\frac{1}{V}\right)^2 + \left(\frac{\Delta\theta}{\Delta\lambda}\right)^2}{\left(1 - \frac{\Delta V}{\Delta\lambda}\cdot\frac{1}{V}\right)^2 + \left(\frac{\Delta\theta}{\Delta\lambda}\right)^2}} \tag{2.21}$$

The ideal value of LTI occurs by evaluating the limit of the expression in (2.21) as $\Delta\lambda \rightarrow 0$ and the terms $\Delta V/\Delta\lambda$ and $\Delta\theta/\Delta\lambda$ become $dV/d\lambda$ and $d\theta/d\lambda$, respectively. The terms $dV/d\lambda$ and $d\theta/d\lambda$ are the sensitivities of the voltage magnitude and the phase angle with respect to the load scaling factor. Hence, the proposed index is termed as the Sensitivity-based Thevenin Index (STI), to indicate that it connects sensitivity and the Local Thevenin Index. The expression of the STI is presented in Eq. (2.22) [26].

$$\mathrm{STI} = \lim_{\Delta\lambda\rightarrow 0} \mathrm{LTI}\,(\Delta\lambda) = \sqrt{\frac{\left(\frac{dV}{d\lambda}\cdot\frac{1}{V}\right)^2 + \left(\frac{d\theta}{d\lambda}\right)^2}{\left(1 - \frac{dV}{d\lambda}\cdot\frac{1}{V}\right)^2 + \left(\frac{d\theta}{d\lambda}\right)^2}} \tag{2.22}$$

The terms $dV/d\lambda$ and $d\theta/d\lambda$ are well known in industry and academia and similar sensitivities have been conventionally used as voltage stability indicators at the control center, before the widespread deployment of PMUs [27]. As the above derivation shows, there is a direct connection between the LTI and the sensitivities and hence the LTI can also be used as an indicator of static long-term voltage stability. Intuitively, the reason for using the sensitivities can be understood using Fig. 2.21 which shows a *P*-*V* curve with three operating points Point A, B, and C. Point A is the present operating point, point B corresponds to a negative load increment ($\Delta\lambda < 0$), and point C corresponds to a positive load increment ($\Delta\lambda > 0$). The LTI derived using the $\Delta\lambda$ is directly related to the slope of the secants AB or AC. As the ideal value of the LTI occurs when the $\Delta\lambda \rightarrow 0$, this corresponds to the slope of the tangent at point A (which is the same as the sensitivity). Thus, the sensitivities at an operating condition can be used to calculate the ideal LTI at a particular bus.

The calculation of the sensitivities in power systems is a standard procedure and requires the Jacobian at an operating point [28]. Let $f\left(\overline{V}, \overline{\theta}\right)$ be the set of expressions for the active power injection at all PV and PQ buses and let $g\left(\overline{V}, \overline{\theta}\right)$be the set of expressions for reactive power injection at all PQ buses. The sensitivities are determined by solving the linear system of equations given in (2.23).

$$\begin{bmatrix} f_{\overline{\theta}} & f_{\overline{V}} & \overline{P}_{\lambda} \\ g_{\overline{\theta}} & g_{\overline{V}} & \overline{Q}_{\lambda} \\ 0 & 0 & 1 \end{bmatrix} \cdot \begin{bmatrix} d\overline{\theta} \\ d\overline{V} \\ d\lambda \end{bmatrix} = \begin{bmatrix} 0 \\ 0 \\ 1 \end{bmatrix} \tag{2.23}$$

The submatrices $f_{\overline{\theta}} \& f_{\overline{V}}$ are the partial derivatives of the active power flow injection expressions with respect to the angles and voltages and can be extracted

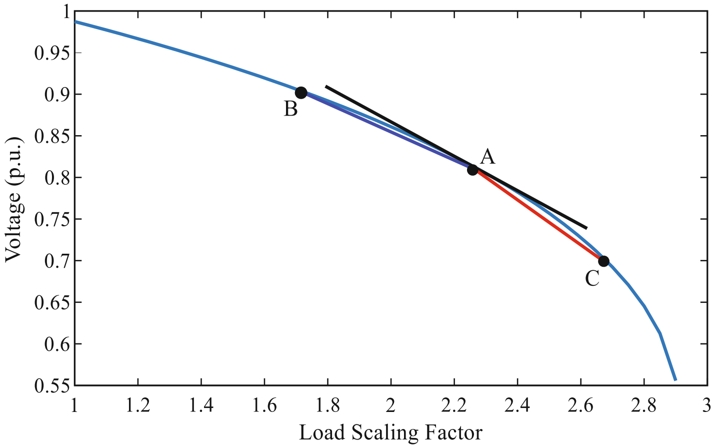

Fig. 2.21 A *P*-*V* curve indicating that the slope of tangent at a Point, A, is between the slope of secants, AB ($\Delta\lambda < 0$) and AC ($\Delta\lambda > 0$)

directly from the power system Jacobian at that operating point. Similarly, $g_{\overline{\theta}}$ &$g_{\overline{V}}$ correspond to the partial derivatives of the reactive power flow and are similarly extracted from the Jacobian. P_λ and Q_λ are column vectors and correspond to how the active and reactive power injections vary as a function of $\Delta\lambda$. As described before, the voltage sensitivity at an operating point is essentially the slope of the tangent of the P-V curve at that point and this method to determine sensitivities is numerically robust to noise, compared to numerically computing $\Delta V/\Delta\lambda$.

2.6.4 Incorporating the Distribution Network in Thevenin Index

One of the key assumptions in the Thevenin Equivalent-based methods using PMU measurements [17–20, 22–26] is that the load is connected to the transmission system. In reality, the loads are located in the sub-transmission and distribution networks and this has to be incorporated into the Thevenin Equivalent. This is conceptually done in the modified Thevenin equivalent represented in Fig. 2.22 where the impedance $\boldsymbol{Z}_{eq_D}$ represents an aggregation of the distribution feeders in a load area and the equivalent load impedance is given by $\boldsymbol{Z}_{L_D}$. The parameters of the modified Thevenin Equivalent can be estimated from quasi-steady-state voltage and current phasor measurements in the transmission and distribution system. More details about the parameter estimation can be found in [29].

Comparing the two equivalents in Figs. 2.20 and 2.22, it can be seen that$\boldsymbol{Z}_L = \boldsymbol{Z}_{L_D} + \boldsymbol{Z}_{eq_D}$. As the load is present at the distribution node, at the critical loading $\left|\boldsymbol{Z}_{L_D}\right| = \left|\boldsymbol{Z}_{eq_T} + \boldsymbol{Z}_{eq_D}\right|$. Combining this information with it can be deduced that the LTI calculated at the transmission bus is the Thevenin equivalent including the distribution network equivalent is less than 1. The new voltage stability index ($\mathrm{VSI_D}$) that accounts for the distribution network is given in Eq. (2.24) [29]. It is shown in [29] that this index successfully identifies the critical loading for T&D co-simulated systems [12] while the previous index LTI cannot identify it due to the absence of a distribution network representation in Fig. 2.20. The Thevenin equivalent in Fig. 2.22 can be used to represent three-phase unbalanced circuits in which the equivalent parameters ($\boldsymbol{E}_{eq}, \boldsymbol{Z}_{Eq_T}, \boldsymbol{Z}_{eq_D}$&$\boldsymbol{Z}_{L_D}$) are all in three-

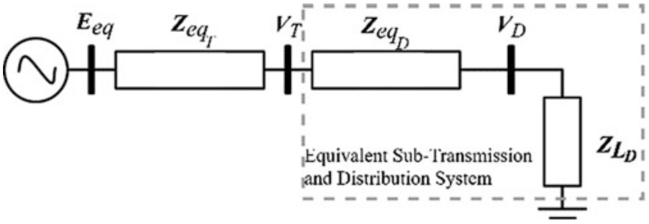

Fig. 2.22 Structure of the modified Thevenin Equivalent including the distribution network

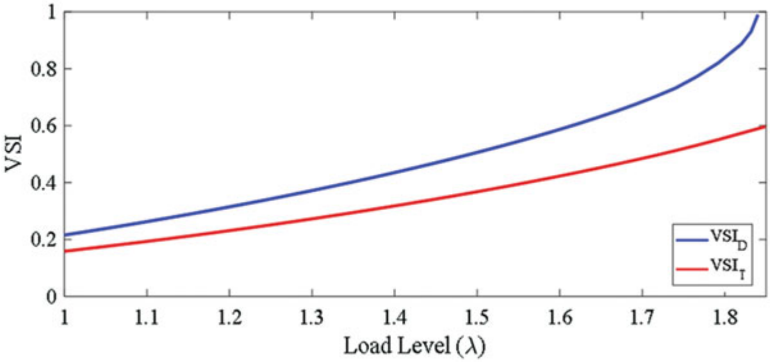

Fig. 2.23 $\mathrm{VSI}_{\text{D-}3\phi}$ at critical node in distribution network and VSI_T at corresponding transmission node vs. load scaling (extract from [29])

phase representation [29]. The VSI in (2.24) can be extended for the three-phase equivalents ($\mathrm{VSI}_{\text{D-}3\phi}$) to identify the critical loading for three-phase circuits by comparing the losses in the networks with the load power and is shown in Eq. (2.25). More details on the estimation of the three-phase Thevenin Equivalent parameters using three-phase quasi-steady-state voltage and current phasor measurements in the transmission and distribution system can be found in [29].

$$\mathrm{VSI}_\mathrm{D} = \frac{\left|\boldsymbol{Z}_{eq_T} + \boldsymbol{Z}_{eq_D}\right|}{\left|\boldsymbol{Z}_{L_D}\right|} \tag{2.24}$$

$$\mathrm{VSI}_{D-3\phi} = \frac{\left|\boldsymbol{S}_{\mathrm{loss}_{T-3\phi}} + \boldsymbol{S}_{\mathrm{loss}_{D-3\phi}}\right|}{\left|\boldsymbol{S}_{L_{D-3\phi}}\right|} \tag{2.25}$$

To validate the methodology, co-simulation is used for identifying the critical loading on the test system. The test system has IEEE 9 bus as the transmission network with the loads at all three load buses (5, 7, and 9) replaced with the IEEE 13 bus distribution test feeders [29]. The critical nodes are in the distribution system connected to Bus 5 with a critical loading $\lambda = 1.85$. Figure 2.23 plots the $\mathrm{VSI}_{\text{D-}3\phi}$ at the critical node in distribution network and the VSI at the transmission bus as the loading in the system increases. It can be seen that the value of the $\mathrm{VSI}_{\text{D-}3\phi}$ reaches the critical value of 1 while the value of the VSI at the transmission bus only reaches a value of 0.6. Thus, only using the PMU measurements from the transmission system can lead to situations where the voltage instability is not detected/identified. This drawback can be mitigated by using measurements from distribution system are used and by accounting for the three-phase unbalanced nature of the distribution system in the Thevenin Equivalent [29].

The modified Thevenin Equivalent including the distribution network along with the $\mathrm{VSI}_{\text{D-}3\phi}$ can also be used for offline studies with a co-simulation setup

[12] to identify the critical nodes in the distribution system and the overall T&D system [29]. Further, there have been scenarios when the overall system has been distribution limited [30]. The modified Thevenin Equivalent is able to distinguish between the transmission limited and distribution limited system [29].

2.7 Short-Term Voltage Stability

The phenomenon of voltage stability in the time scale of up to 30 s is referred to as short-term voltage stability as the dynamics involved are very different from the dynamics and components involved in long-term voltage stability. Short-term voltage stability involves dynamics of fast-acting load components such as induction motors, electronic loads, HVDC links, and inverter-based generator resources. The study period of interest is in the order of several seconds and so detailed models that can represent power system transient dynamics are critical. For short-term voltage stability, the dynamic modeling of loads is essential, and short circuit faults near loads are the main concern [1].

The typical case of short-term voltage instability is the stalling of induction motors (IM) after a large disturbance (such as a fault of a loss of generation) either due to the loss of equilibrium between electromagnetic and mechanical torques in the induction motor or due to escaping the region of attraction of the stable equilibrium due to delayed fault clearing [1]. During a fault, induction motors decelerate due to decreased electromagnetic torque, which makes them draw higher current and much larger reactive power, causing further voltage depression. After fault clearing, the load voltage partially recovers and the electromagnetic torque improves. If the motor has not decelerated below a critical speed, it reaccelerates towards the normal operating rotational speed and the load voltage returns to the nominal value. If the motor has decelerated below a critical speed, it cannot reaccelerate and the motor decelerates to a stop (stalls). Stalled motors can either be disconnected by undervoltage protections or remain connected, drawing a large (starting) current until they are disconnected by thermal overcurrent protections. If the stalled motors remain connected, the voltage remains depressed for a longer time (>10 s), possibly inducing a cascade of stalling on nearby motor loads. This mode of short-term voltage instability also applies to induction generators. The difference is that induction generators accelerate instead of stalling during faults and, if unstable, they are disconnected by overspeed relays instead of undervoltage relays.

2.7.1 Fault Induced Delayed Voltage Recovery

Single-phase induction motors that are often used in residential air-conditioners are more susceptible to stalling than large three-phase induction motors due to their smaller inertia [31, 32]. The stalling of large numbers of single-phase induction

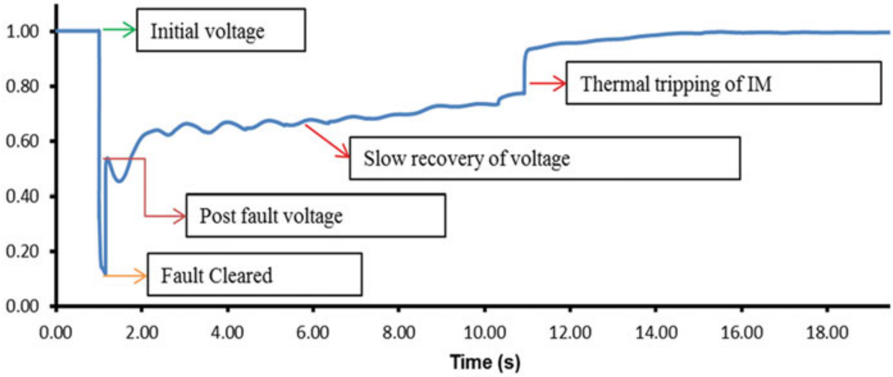

Fig. 2.24 Conceptual FIDVR waveform at a bus

motors leads to a phenomenon referred to as Fault Induced Delayed Voltage Recovery (FIDVR) [31, 33]. In FIDVR events, the eventual tripping of the stalled motors is also through the thermal protection of the individual motors. FIDVR is also a potential cause of cascading and/or instability depending on the network topology and available reactive support close to the event.

FIDVR is mainly caused in systems with a moderate amount of single-phase (1ϕ) induction motor loads (2530%). After a large disturbance (fault, etc.), these motors, that are connected to mechanical loads with constant torque, stall and typically draw 5–6 times their nominal current and this leads to the depression of the system voltage for a significant amount of time. The low voltages in the system inherently lead to some load being tripped by protection devices close to the fault. However, even after this, the concern is that the sustained low voltages (>10 s) can lead to cascading events in the system steering towards a blackout. A typical delayed voltage response after a fault along with the various features is shown in Fig. 2.24. In this particular example, all the IMs are tripped at the same time, leading to a sudden voltage recovery. There can also be scenarios in which the thermal tripping is more gradual, leading to a gradual voltage recovery.

Most single-phase induction motor are used in residential air-conditioners and so the FIDVR phenomenon has been historically observed in systems where a large number of residential AC’s are operational at the same time (e.g., summer in California or Arizona). Most of these devices do not use undervoltage protection schemes and are only equipped with the thermal protection with an inverse time-overcurrent feature, delaying the tripping up to 20 s.

2.7.2 FIDVR Events Observed

Description of several FIDVR events observed in the field are listed in [34] and almost all of them occur in high residential load areas during a period of high temperature. As an example, Fig. 2.25 shows an FIDVR event on a 115 kV bus in Southern California on July 24, 2004. The sustained low voltage is likely caused by stalled AC IM's and the voltage finally recovered to pre-contingency voltage around 25 s after the fault. Out of the substation load of 960 MW, 400 MW of load was tripped by protection devices in residential and commercial units to recover the voltage.

FIDVR can also occur in distribution feeders due to lightning strikes on the feeders. An FIDVR event occurred on July 10, 2012, in the Southern California Edison System and lasted approximately 9 s [35]. This FIDVR event occurring in a single distribution feeder was detected using micro-PMUs [36] in the distribution feeder at Valley substation. The nominal power is 30 kW and so this micro-PMU essentially monitors the behavior of around 10–15 households. The purpose of the micro-PMUs is to capture load events and to enable proper load modeling. Lightning strikes caused multiple distribution faults and reduced voltage to 60% causing some loads to stall. The stair-shaped profile for real power indicates that several loads disconnected approximately 6 s after the FIDVR event was initiated and is due to thermal protection schemes tripping off residential A/C units. The voltage profile shown in Fig. 2.26 (Fig. 6.1 in [35]) is not so flat and there are several voltage sags (e.g., at 5 s) which make it hard to quantify FIDVR just from voltage.

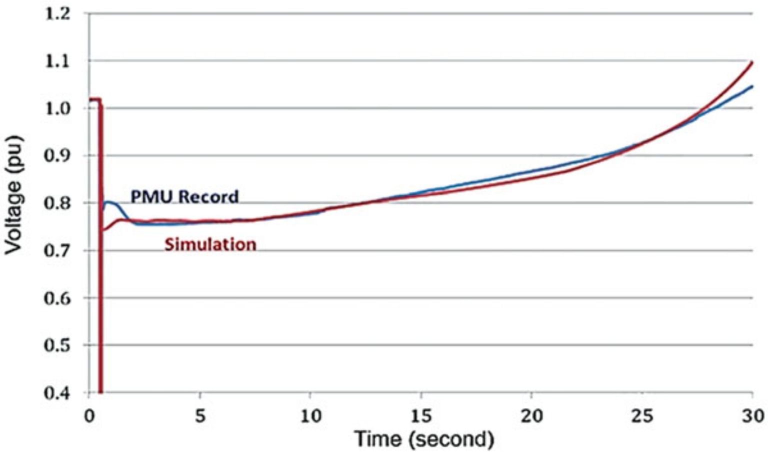

Fig. 2.25 Recorded delayed voltage recovery waveform at a 115kv bus in southern California on July 24, 2004 [34]

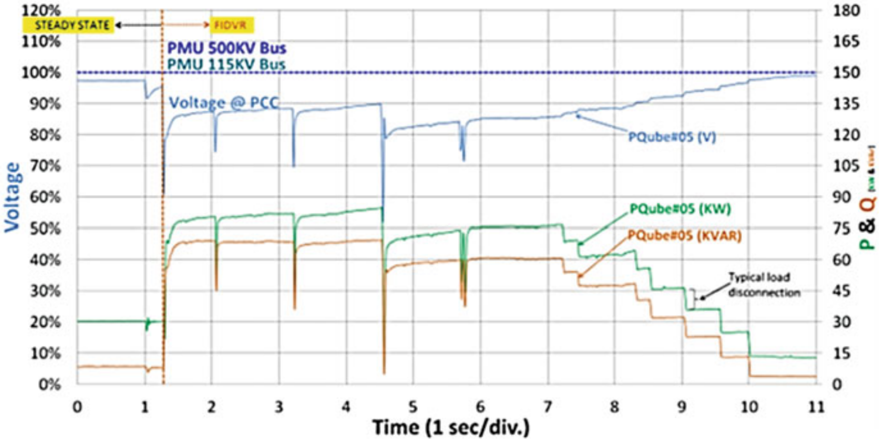

Fig. 2.26 Voltage, active power, and reactive power for the SCE FIDVR event on July 10, 2012. (extract from [35])

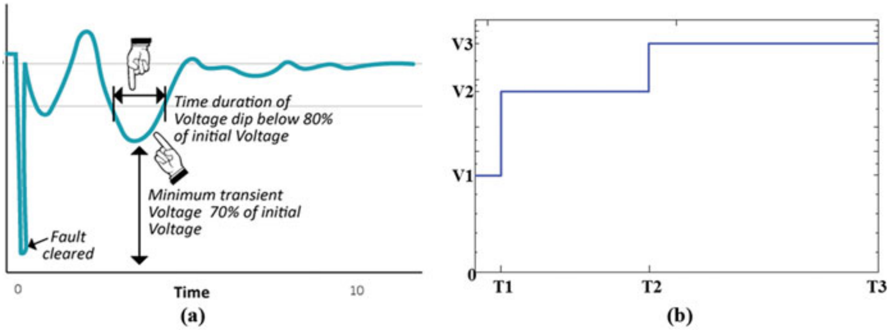

Fig. 2.27 (**a**) WECC transient voltage criteria [37] (**b**) simplified voltage criteria [38]

2.7.3 *Transient Voltage Criteria*

To prevent uncontrolled loss of load in the bulk electric system, NERC, WECC, and other regulatory bodies have specified transient voltage criteria that utilities and system operators need to satisfy after a fault has been cleared. Figure 2.27 provides a pictorial representation of the WECC criteria [37] and the simplified voltage criteria (PJM criteria [38]).

The WECC transient criteria is defined as the following two requirements [37]

1. Following fault clearing, the voltage shall recover to 80% of the pre-contingency voltage within 20 s of the initiating event.
2. Following fault clearing and voltage recovery above 80%, voltage at each applicable bulk electric bus serving load shall neither dip below 70% of

pre-contingency voltage for more than 30 cycles nor remain below 80% of pre-contingency voltage for more than 2 s.

A simplified voltage criteria is used generally by utilities and the trajectory of the recovering voltage must be above the curve in Fig. 2.3b where $V_1 = 0.5$, $V_2 = 0.7$ & $V_3 = 0.95$ and $T_1 = 1\ s$, $T_2 = 5\ s$ & $T_3 = 10\ s$. The ERCOT criteria for transient voltage response requires that voltages recover to 0.90 p.u. within 10 s of clearing the fault [39]. The utilities ensure that the voltage recovery satisfies the guidelines specified by their regulatory authority during their planning phase and operational phase by either installing VAR devices (STATCOM, SVC, etc.) in critical regions and by ensuring that sufficient dynamic VARS are available during operation. In order to study the phenomenon of short-term voltage instability in practical systems, power system time domain simulators are used along with the appropriate load models that can accurately model the phenomenon. This is described in the next section.

2.8 Dynamic Composite Load Model by WECC

In order to enable the utilities and system operators to simulate the transient voltage phenomenon and estimate the amount of VAR support required to prevent short-term voltage stability issues, a dynamic load model has been developed recently by WECC called as the Dynamic Composite Load Model [40]. The composite model essentially aggregates the various kinds of dynamic loads in the sub-transmission network into several 3-ϕ IM (representing high, medium, and low inertias) and an aggregate 1-ϕ IM (representing the AC loads). Furthermore, the protection schemes that trip a proportion of the loads are also implemented for each of the motor representing the Undervoltage and Underfrequency protection policies. An equivalent feeder is also present that tries to emulate the impact of voltage drop in the distribution system when a large current is drawn. The overall structure of the composite load model is shown in Fig. 2.28.

This model has 132 parameters and has been implemented by vendors in commercial software such as PSSE, PSLF, and PowerWorld. More details along with descriptions of the various parameters can be found in [40]. The various components of the composite load model are explained in the next subsections.

2.8.1 Substation and Feeder Model

The substation transformer is modeled as an on-load tap changing (LTC) transformer that can regulate its low-side voltage. A compensating impedance is used to represent line-drop compensation. A single shunt capacitor is represented on the low-side bus with a susceptance (Bss) to account for the capacitors in the distribution

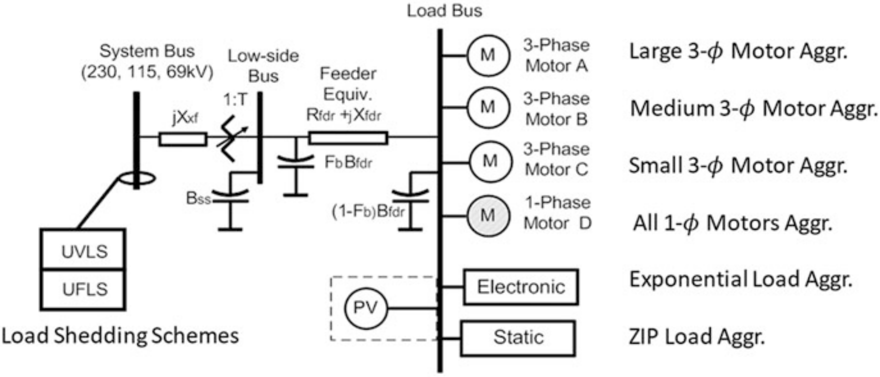

Fig. 2.28 Structure of the composite load model [40]

and sub-transmission systems. The feeder equivalent includes series resistance and reactance and shunt capacitors at both ends to capture the line charging of the individual feeders in the distribution and sub-transmission system.

2.8.2 Static and Electronic Load Models

The static load model is represented as either ZIP loads or as exponential load models [40] whose parameters are input by the user. The electronic load model is represented as a constant power load with an additional logic to reduce the load when the load voltage falls below a user-defined setpoint. These loads are not the main contributors in the short-term voltage stability phenomenon.

2.8.3 Three-Phase Induction Motor Load Model

The three-phase (3ϕ) induction motor (IM) is a highly dynamic load, and therefore it needs to be properly represented with detailed differential and algebraic equations. A standard way to model the 3-ϕ IM is by an equivalent circuit [41] where the stator and rotor impedances along with the mutual inductances are specified. A summary of the governing equations of a single cage three-phase IM is given in Eq. (2.26).

$$
\begin{aligned}
\frac{d\phi_{ds}}{dt} &= \omega_b \left[V_{ds} - R_s \cdot \frac{X_r}{X_e^2} \cdot \phi_{ds} - \phi_{qs} + R_s \cdot \frac{X_M}{X_e^2} \cdot \phi_{dr} \right] \\
\frac{d\phi_{qs}}{dt} &= \omega_b \left[V_{qs} - R_s \cdot \frac{X_r}{X_e^2} \cdot \phi_{qs} + \phi_{ds} + R_s \cdot \frac{X_M}{X_e^2} \cdot \phi_{qr} \right] \\
\frac{d\phi_{dr}}{dt} &= \omega_b \left[-R_r \cdot \frac{X_s}{X_e^2} \cdot \phi_{dr} - (1 - \omega_r)\, \phi_{qr} + R_r \cdot \frac{X_M}{X_e^2} \cdot \phi_{ds} \right] \\
\frac{d\phi_{qr}}{dt} &= \omega_b \left[-R_r \cdot \frac{X_s}{X_e^2} \cdot \phi_{qr} + (1 - \omega_r)\, \phi_{dr} + R_r \cdot \frac{X_M}{X_e^2} \cdot \phi_{qs} \right] \\
\frac{d\omega_r}{dt} &= \frac{1}{H} \left[\frac{X_M}{X_e^2} \left(\phi_{ds} \cdot \phi_{qr} - \phi_{dr} \cdot \phi_{qs} \right) - T_L \cdot \omega_r^{T_e} \right]
\end{aligned}
\tag{2.26}
$$

where the states of the dynamic model are ϕ_{ds}, ϕ_{qs}, ϕ_{dr} & ϕ_{qr} which correspond to the flux linkages along the d and q axis of the stator and rotor and the rotor speed (ω_r). R_r, R_s, X_r, X_s, X_M and H are the parameters of the induction motor with $X_e = \sqrt{X_s X_r - X_M^2}$ and ω_b is the synchronous rotor speed. T_L is the mechanical load torque coefficient and T_e is the mechanical load torque exponent (In practice $T_e < 2$). The input to this model are the voltages that are on the stator side and are V_{ds} & V_{qs} which correspond to the d- and q-axis components of the grid voltage. The active and reactive power consumed by the IM model can be written in terms of the states and the inputs and is given by Eq. (2.27).

$$
\begin{aligned}
P &= \frac{V_{ds}}{X_e^2} \cdot (X_r \cdot \phi_{ds} - X_M \cdot \phi_{dr}) + \frac{V_{qs}}{X_e^2} \cdot \left(X_r \cdot \phi_{qs} - X_M \cdot \phi_{qr} \right) \\
Q &= \frac{V_{ds}}{X_e^2} \cdot \left(X_r \cdot \phi_{qs} - X_M \cdot \phi_{qr} \right) - \frac{V_{qs}}{X_e^2} \cdot (X_r \cdot \phi_{ds} - X_M \cdot \phi_{dr})
\end{aligned}
\tag{2.27}
$$

In most practical systems, the induction motor is a double cage model of either type-1 or type-2. The equivalent circuits of the two types of three-phase double cage induction motors are shown in Fig. 2.29. In order to apply the Eqs. (2.26) and (2.27) to the double cage model, the equivalent rotor resistance (R_r) and reactance (X_r) is calculated as a function of the rotor speed (ω_r) and the rotor parameters. More details can be found in [41].

The 3-ϕ IM components in the composite load model are specified by the transient and sub-transient parameters and not the impedances. The transient and sub-transient parameters (Ls, Lp, Lpp, Tp0, and Tpp0) can be determined from

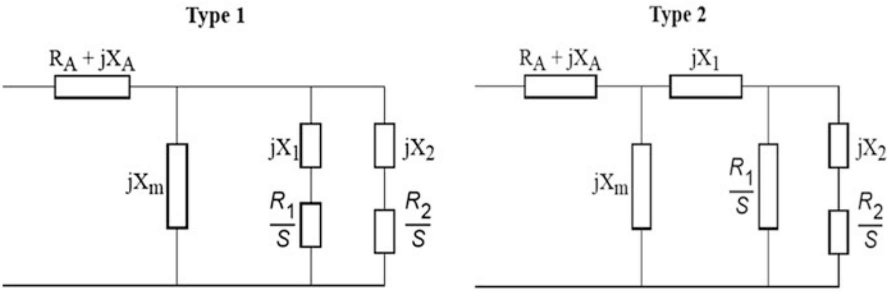

Fig. 2.29 Equivalent circuits of the two types of three-phase double cage induction motors

the impedance parameters of the standard model using the relations in Eq. (2.28) [42] where the terms X_m, X_A, X_1, X_2, R_A, R_1 & R_2 correspond to the components indicated in Fig. 2.29.

$$\begin{aligned}
&L_s = (X_A + X_m)\,/\omega_{\text{base}}\\
&L_p = (X_A + (X_1 \cdot X_m)\,/\,(X_1 + X_m))\,/\omega_{\text{base}}\\
&L_{pp} = (X_A + (X_1 \cdot X_2 \cdot X_m)\,/\,(X_1 \cdot X_2 + X_2 \cdot X_m + X_m \cdot X_1))\,/\omega_{\text{base}}\\
&T_{p0} = (X_1 + X_m)\,/\,(\omega_{\text{base}} \cdot R_1)\\
&T_{ppo} = (X_2 + (X_1 \cdot X_m)\,/\,(X_1 + X_m))\,/\,(\omega_{base} \cdot R_2)
\end{aligned} \tag{2.28}$$

The 3-ϕ IM model is also equipped with two undervoltage relays that are activated cumulatively based on the user settings. Appropriate settings of the undervoltage relays prevent short-term instability due to the stalling of the 3ϕ IM.

2.8.4 Single-Phase Induction Motor Load Models

The 1ϕ IM A/C performance-based model was developed by Western Electricity Coordinating Council (WECC) Load Modeling Task Force members based on extensive laboratory testing of a variety of A/C units. The model represents the combined positive sequence phasor behavior of several individual single-phase A/C compressors and can represent complex behavior such as

1. Stalling the compressor motors when the node voltage is below a threshold value (V_{stall}) for more than a pre-specified time (t_{stall}).
2. Restarting a fraction of the A/C load if the voltage recovers above a set value (V_{rst}) for more than a pre-specified time (t_{rst}), i.e., these motors are no longer stalled. This fraction is set by a parameter F_{rst}.
3. Disconnection of the stalled motors due to thermal protection after a few seconds. This is controlled by a thermal relay.

Figure 2.30 shows the block diagram of the 1ϕ IM A/C model and demonstrates how the active and reactive power demanded is dependent on the node voltage (V) and frequency (F). The thermal relays are only activated when stalling occurs and are inactive in normal operation. The circles with Π & Σ correspond to multiplication and addition, respectively. It can be seen that the compressor motor model is divided into two parts:

(a) Motor A—Those compressors that cannot restart after stalling and remain stalled even after the voltage rises above the stall voltage.
(b) Motor B—Those compressors that can restart after stalling if the voltage rises above a certain setpoint.

The motors A and B are represented by algebraic Eqs. (2.29) and (2.30) that describe the variation of the active power and reactive power load with the load bus

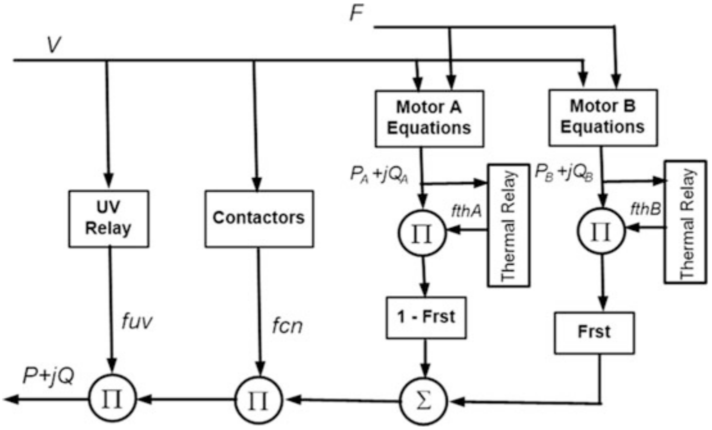

Fig. 2.30 The block diagram of the 1ϕ IM A/C model with various components [40]

voltage (V) and the frequency (F) per unit. The active and reactive powers of the motors A and B are scaled by $(1 - F_{rst})$ and F_{rst}, respectively before being added to get the final power of the 1ϕ IM A/C model. The various symbols in the Eqs. 2.29 and 2.30 such as V_{brk}, K_{p1}, N_{p1}, G_{stall} are all parameters of the composite load model and are provided by the user.

$$P = \begin{cases} P_0 + K_{p1}\,(1 + (F - 1))\,(V - V_{brk})^{N_{p1}} & V > V_{brk} \\ P_0 + K_{p2}\,(1 - 3.3\,(F - 1))\,(V - V_{brk})^{N_{p2}} & V_{\text{stall}} < V < V_{brk} \\ G_{\text{stall}} \cdot V^2 & V < V_{\text{stall}} \end{cases} \tag{2.29}$$

$$Q = \begin{cases} Q_0 + K_{q1}\,(1 + (F - 1))\,(V - V_{brk})^{N_{q1}} & V > V_{brk} \\ Q_0 + K_{q2}\,(1 - 3.3\,(F - 1))\,(V - V_{brk})^{N_{p2}} & V_{\text{stall}} < V < V_{brk} \\ B_{\text{stall}} \cdot V^2 & V < V_{\text{stall}} \end{cases} \tag{2.30}$$

The motors stall when the voltage at the node becomes less than V_{stall} for more than t_{stall} seconds and this activates the thermal relay. The fraction of motors A and B connected after stalling is determined by the fraction f_{th} which is the output of the thermal relay. The power demanded by the motors are then scaled by the fractions fcn and fuv that correspond to the reduction in power due to contactors and undervoltage protection.

The 1-ϕ induction motor is the main reason why the FIDVR is observed. The 1-ϕ IM model has representations of the AC compressor motor, compressor motor thermal relay, undervoltage relays, and contactors. Depending upon the input voltage, the motor operates either in "running" or "stalled" state. The behavior of the motor as a function of the voltage can be understood based on the power consumption of the motor. Figure 2.31 plots the active and reactive power demand as a function of the voltage for the normal operation and stalled operation. From

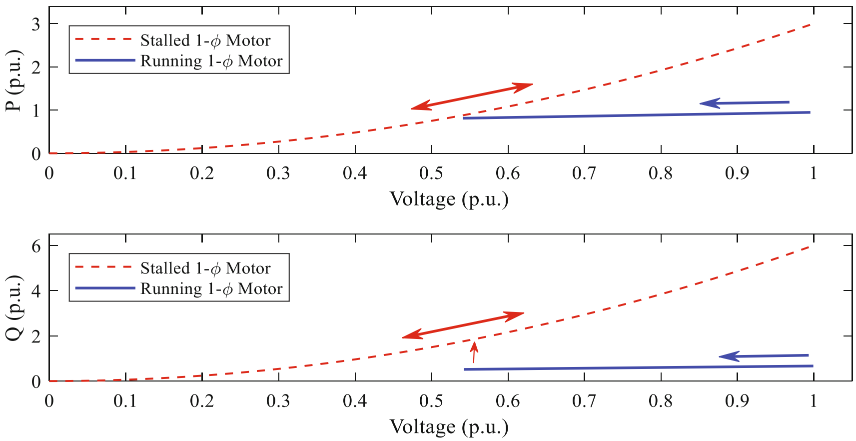

Fig. 2.31 Active power (Top) and reactive power (Bottom) versus the voltage for the normal operation (Blue) and stalled operation (Red) for the 1-Φ induction motor [43]

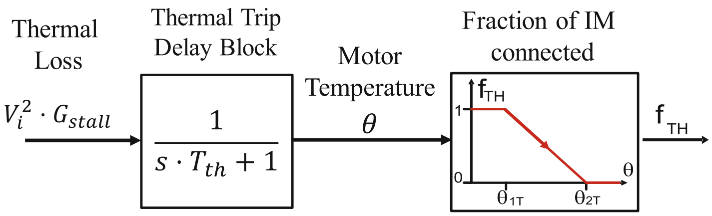

Fig. 2.32 The structure of thermal relay in the 1ϕ IM A/C model [40]

Fig. 2.31, it can be seen that in the stalled state, the active power demand is three times the nominal amount and the reactive demand is six times the nominal amount compared to the normal "running" state. This large demand is the reason why the voltage reduces at the substation causing FIDVR. This demand naturally is reduced via thermal protection that takes around 10–15 s.

The thermal relay block diagram is shown in Fig. 2.32, where $V_i^2 \cdot G_{\text{stall}}$ is the thermal power dissipated in the motor. T_{th} is the thermal relay time constant and θ is the motor temperature estimated by the relay. Initially, the internal temperature is zero and the thermal loss is zero. As the stalling condition occurs suddenly, the input to the thermal delay block can be approximated by a step function and the temperature (θ) rises in an exponential manner. The f_{th} fraction remains 1 till the temperature reaches θ_1 after which the fraction reduces linearly with the temperature until the temperature reaches θ_2 when all the motors are disconnected. A more analytical description of the rise of motor temperature can be found in [43, 44].

It can be seen from the equations and the description that the 1ϕ IM A/C model is highly nonlinear and has complex dynamics (stalling, restarting, thermal disconnection) with conditional arguments. These complex dynamics make the study and control of FIDVR challenging.

2.8.5 *Key Parameters for the Composite Load Model*

One of the key challenges for the utilities in the simulation of the composite load model by utilities is a large number of parameters (130+) of the model. To aid the utilities in their dynamic studies WECC has provided default parameters that are derived from the study of several feeders in their footprint [32, 40]. Furthermore, the US Department of Energy in conjunction with the WECC's Load Modeling Task Force has developed a tool to identify the parameters of the composite load model based on the geographic location of the feeder. The Load Model Data Tool [44] is available for utilities to create the composite load model dynamics file either in PSSE or PSLF compatible format based on the local weather and loading of the feeder.

Another method to estimate the model parameters is to use recorded FIDVR events at a substation and then utilize parameter estimation techniques [46] as the structure of the model is known. However, a large number of parameters make the problem ill-defined. To solve this issue, most of the parameters are fixed to be the same as the default values (or the values from the Load Model Data Tool) and only a few key parameters that impact the load dynamics behavior are chosen for the parameter estimation. The key parameters of the composite load model have been identified from sensitivity studies [47] and are the following:

- Stall voltage in p.u. (Vstall).
- Stall time delay in sec. (Tstall).
- Motor D fraction of load power (FmD).
- Fraction of load with undervoltage relay protection (Fuvr).
- Motor D thermal time constant in sec. (Tth).
- Motor D thermal protection trip start level (Th1t).
- Motor D thermal protection trip completion level (Th2t).

The report [47] also provides the key parameters of the three-phase motors in the composite load model and recommends Transmission Owners and Transmission Planners focus data collection on the key parameters.

2.9 Data-Driven Methods to Assess and Monitor Short-Term Voltage Stability

Once the modeling of the power system components is complete, the time domain power system simulators are used to perform various contingency studies under different plausible operating scenarios and load behaviors. The results of these simulations are then used for identifying regions in the power system that are susceptible to short-term voltage instability [48]. One challenge in directly utilizing the time series data is that the characterization of the stability/instability of a particular time domain simulation from the resulting data is not trivial and needs

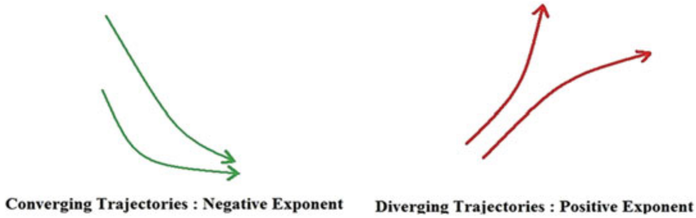

Fig. 2.33 Convergent and divergent trajectories and corresponding sign of Lyapunov exponents

to be done in a systematic manner using methods from control system theory. The Lyapunov Exponent (LE) [49, 50] has been shown to be the appropriate tool for the identification of stability/instability from time series data.

The Lyapunov exponent (LE) is an idea that is adapted from the ergodic theory of dynamical systems. The maximum Lyapunov exponent is a measure of the rate of separation of two trajectories in the system and is used to ascertain the system stability. If the maximum Lyapunov exponent is negative, the trajectories of the system converge to a stable equilibrium. However, if the maximum Lyapunov exponent is positive, the trajectories of the system diverge; this suggests a possibly unstable and chaotic system. This is illustrated in Fig. 2.33.

2.9.1 *Computation of Lyapunov Exponent from Time Series Data*

The algorithm for the computation of the maximum LE based on the voltage time series data is outlined below [49, 50]:

1. Let $V(t)$ be a vector of voltages at different buses at time t. The voltages are sampled at a constant sampling frequency Δt. Thus, $t = 0, \Delta t, 2\Delta t, \ldots.$
2. The values of ϵ_1 and ϵ_2, which are fixed in advance, determine when the algorithm is initialized. Choose integer N such that $\epsilon_1 < \|V(m\Delta t) - V((m-1)\Delta t)\| < \epsilon_2$ for $m = 1, 2, \ldots, N$; $0 < \epsilon_1 < \epsilon_2$.
3. The maximum LE of the system at time $k\Delta t$ can be calculated using the following formula for $k = 1, 2 \ldots.$

$$\Lambda\left(k\Delta t\right) = \frac{1}{Nk\Delta t}\sum_{m=1}^{N}\log\frac{\left\|V\left(\left(k+m\right)\Delta t\right) - V\left(\left(k+m-1\right)\Delta t\right)\right\|}{\left\|V\left(\left(m\right)\Delta t\right) - V\left(\left(m-1\right)\Delta t\right)\right\|} \tag{2.31}$$

The basic idea behind the equation for calculating the LE is that the above equation measures the separation on the voltage trajectories with respect to separation present at the N initial conditions. If the separation of the measurements at a particular instant is lesser than the initial separation then it will result in negative LE, implying converging behavior. If the separation of the measurements at a particular instant is greater than the initial separation then it will result in positive LE, implying diverging behavior. Since the value of the initial separation is used at all the instants to calculate the LE, the selection of the initial points is critical for well-behaved behavior of the algorithm.

The initial points, that determine the initial separation, depend on the values of ϵ_1 and ϵ_2 and so these need to be selected appropriately. These quantities depend on the time difference between consecutive time series data. If the rate at which the measurements are obtained is high, then the change in the value between two consecutive measurements is low. Hence, the values of ϵ_1 and ϵ_2 have to be small. On the other hand, if the measurements are obtained at a low rate, then the values of ϵ_1 and ϵ_2 have to be chosen relatively larger. For simulation purposes, we have measurements at a frequency of 120 Hz. Therefore we chose $\epsilon_1 = 0.002$ and $\epsilon_2 = 0.01$.

The equation to calculate the system-wide LE can be slightly modified to computing the Lyapunov exponent of individual buses to determine the stability/instability contribution of individual buses to the overall system stability/instability. The Lyapunov exponent for the bus will be computed using the following equation.

$$\lambda_{\mathrm{i}}(k\Delta t) = \frac{1}{Nk\Delta t}\sum_{m=1}^{N}\log\frac{\left\| V_i\left(\left(k+m\right)\Delta t\right) - V_i\left((k+m-1)\Delta t\right)\right\|}{\left\| V_i\left(\left(m\right)\Delta t\right) - V_i\left((m-1)\Delta t\right)\right\|} \tag{2.32}$$

Where $V_i((m)\Delta t)$ is the mth sample of voltage measurement at the ith bus and λ_i is the Lyapunov exponent at the ith bus. This is a useful concept as the bus where the exponent is largest is the main contributor to the instability and control actions taken at this bus will have a large impact on the system.

PMU RMS voltage measurements can also be used for the online computation of the Lyapunov exponent using the above formulas is relatively straightforward. The proposed Lyapunov exponent computed, using the voltage measurements from PMU devices at n buses, will provide stability information for all buses whose states can be estimated by using PMU measurements.

2.9.2 Simulation Results for Lyapunov Exponent in PSSE of the 9-Bus System

The WECC 9-Bus system is simulated in PSSE in order to test the Lyapunov exponent methodology described above. A three-phase fault is applied at bus location 5 and the fault is cleared by opening the line 7–5. Two cases of the fault clearing time (t_{cr}) are used—one with a stable scenario (0.05 s) and another with an unstable scenario (0.2 s). The voltage at the various buses for the two cases and the corresponding Lyapunov Exponents are shown in Fig. 2.34.

Simulation results of the WECC 9-Bus system and the IEEE 162-Bus system with different load models and their corresponding LE are described in detail in [49]. It can be observed from the results that the LE settles to a value less than 0 (around -0.5 to be specific) for the scenario when the voltage settles to a steady-state suggesting that the system is stable while the LE settles to a value greater than 0 (around 0.5 to be specific) for the scenario when the voltage is oscillating suggesting that the system is unstable. Thus, the LE is able to correctly predict the stability of the system. Another observation is that the LE sometimes crosses the zero line, changing the estimate of the stability. This is because of the fact that the algorithm presented correctly estimates the actual LE asymptotically, i.e., the estimation becomes better as the time increases. Thus, there is a trade-off between the simulation time and the accuracy of the stability characterization. It is important to note that only the stable cases are affected by this. The unstable case has a positive LE from the start at Bus 5. Thus, there may be situations where the stable cases may be detected as unstable but not the other way around.

2.10 Data-Driven Methods to Assess and Monitor FIDVR

In order to assess and quantify FIDVR from time series data, using only the voltage data might not always be appropriate as the voltage is the result of motor stalling. Thus, quantifying the severity of the stalling is more appropriate for assessing the FIDVR event. One challenge is that the composite load model is too complex for analysis and needs to be simplified. As the thermal relay dynamics is much slower compared to the dynamics of the 3-ϕ IM, the fast dynamics of the 3-ϕ IM can be neglected and only the dynamics of the 1-ϕ IM thermal relay determines the overall behavior of the FIDVR phenomenon. Since the 1-ϕ IM are represented as an admittance after stalling, the 3-ϕ IM and the static loads can also be represented as a voltage-dependent admittance. These observations and modeling assumptions lead to the admittance-based representation of the composite load model.

As a demonstration that the load admittance can indeed capture the load behavior during FIDVR, Fig. 2.35 plots the voltages and Fig. 2.36 plots the load conductance (real component of the admittance) for a normal, moderately severe (30% motor stalling), and very severe (60% motor stalling) delayed voltage recovery after a disturbance. The first observation is the voltage waveforms for both normal recovery and delayed recovery have oscillations due to the behavior of the other components in the system. In comparison, the conductance waveform is much better behaved for the normal recovery and delayed recovery. The oscillations in the voltage are due to the dynamic behavior of the external system (e.g., the generator exciter) and so the impact of these oscillations in the conductance are minimal as the oscillations do not impact the load behavior.

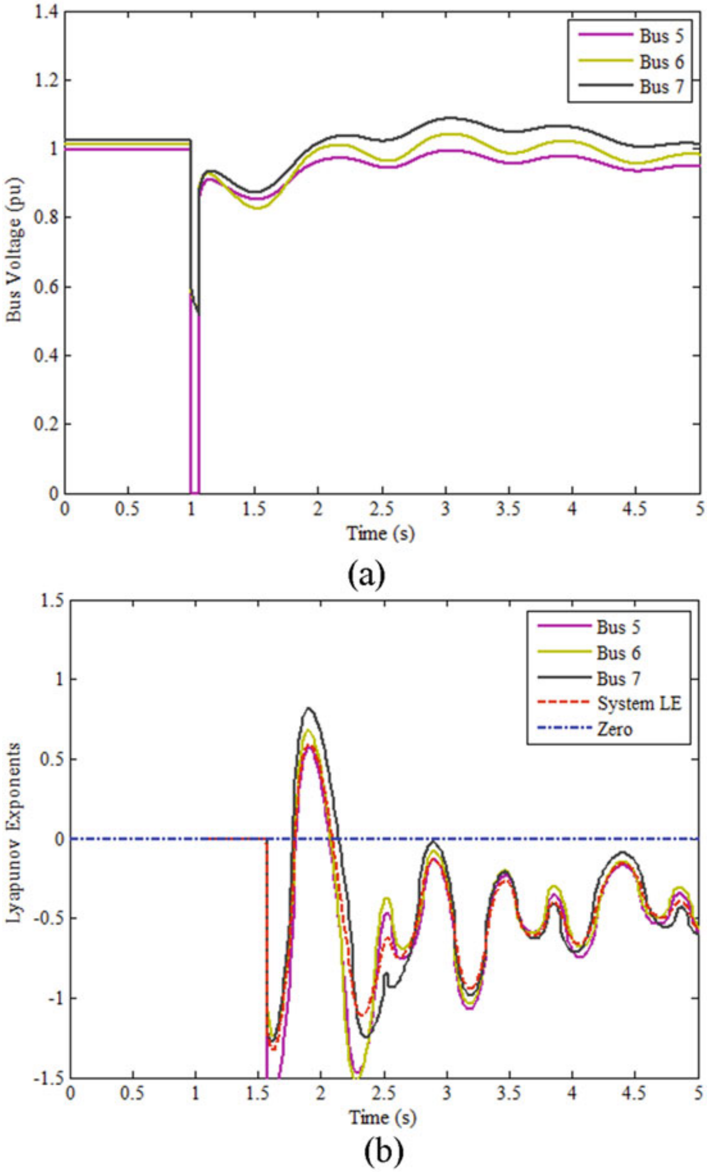

(a)

(b)

Fig. 2.34 The bus voltages and the Lyapunov Exponents for the different fault clearing times leading to stable and unstable scenarios [51]. (**a**) Bus voltage response (t_{cr}=0.05 s). (**b**) Lyapunov Exponent (t_{cr}=0.05 s). (**c**) Bus voltage response (t_{cr}=0.2 s). (**d**) Lyapunov Exponent (t_{cr}=0.2 s)

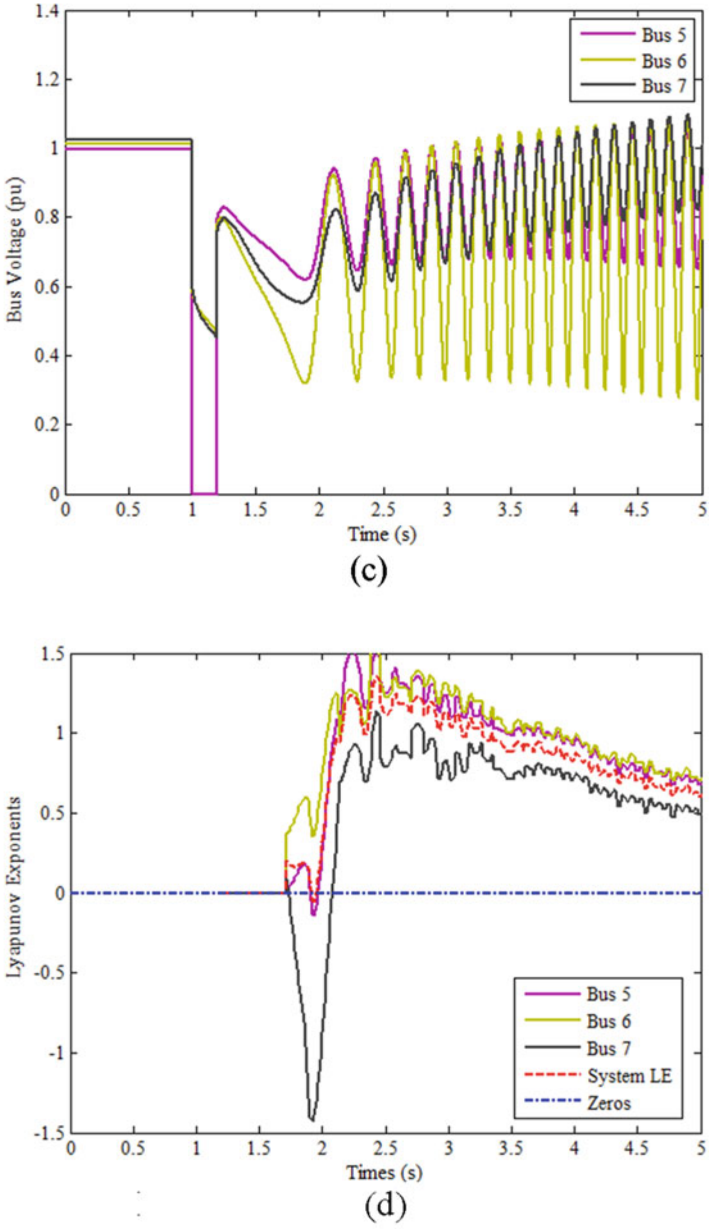

Fig. 2.34 (coninued)

The next observation is that the voltage immediately after the fault is lower for higher amount of motor stalling. Similarly, the load conductance after the fault is cleared increases as the percent of motor stalling increases. However, it is not easy to quantify the severity of the FIDVR event from the voltages as the reduction in

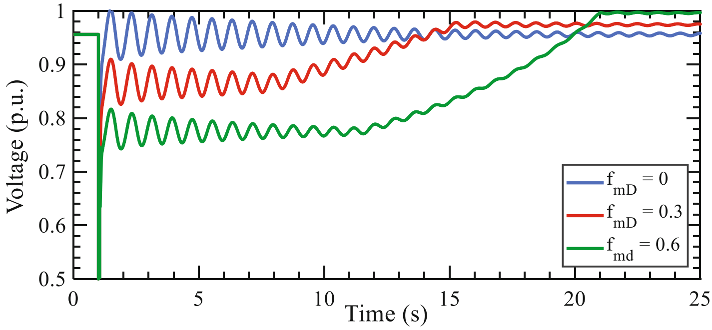

Fig. 2.35 Voltage response with various motor stalling proportion [43]

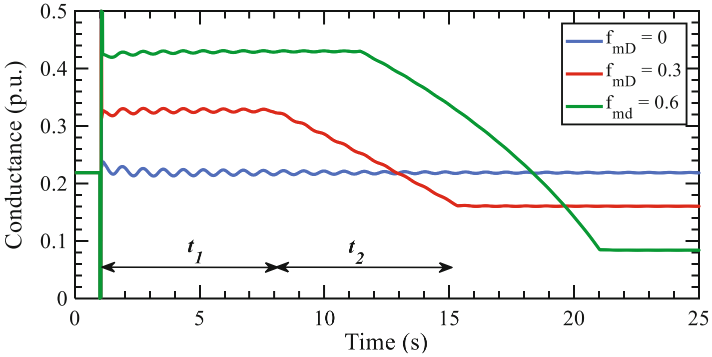

Fig. 2.36 Load conductance with various motor stalling proportion. The times t_1 and t_2 are indicated for $f_{mD} = 0.3$ [43]

voltage is not easily related to the severity and depends on the external network parameters. In contrast, the conductance makes it easy to quantify the severity of the event as the conductance increases in a nearly linear manner to the amount of motors stalled. Thus, it provides a quick way to characterize the severity of the FIDVR and enables monitoring and control schemes based on this quantification. The conductance during normal recovery quickly (<1 s) returns to the pre-contingency value. On the other hand, the conductance of the delayed voltage scenario has a sudden rise due to the stalling of the 1-ϕ IMs.

The sudden rise can be used as a reliable indicator of the onset of the FIDVR phenomenon. The same cannot be said for the voltage as a severe FIDVR on a bus will depress voltages in neighboring buses even if there is no stalling in the neighboring buses. Finally, the conductance for the delayed voltage scenario can be split into two parts—a flat region and a monotonically decreasing region. The flat region corresponds to the time to initiate the thermal tripping of 1-ϕ IM (t_1) and the region where the conductance reduces which corresponds to the time taken to complete the thermal tripping of 1-ϕ IM (t_2). It is much easier to distinguish between these phases of operation from the conductance plots compared to the voltage plots as the oscillations and other phenomena can mask the exact time of transition [43].

The load susceptance has a similar behavior as the load conductance for the FIDVR scenario. By observing various conductance (susceptance) plots for various proportions of stalled motor, two observations can be made: (1) the load conductance (susceptance) is nearly constant till the motor thermal protection triggers and (2) the slope of conductance (susceptance) due to the thermal disconnection is almost constant. Similar observations can be made for FIDVR events in the field both in distribution and transmission systems. For example, Fig. 2.37 plots the load conductance for the FIDVR event described in Fig. 2.26. The conductance plot for the event is less noisy than the voltage plot and also has a similar profile of simulated events (Fig. 2.36). The conductance has a large jump at the stalling condition and is flat till the disconnections begin. The voltage profile (Fig. 2.26) is not flat and there are several voltage sags (e.g., at around 5 s) which make it hard to quantify FIDVR just from voltage. The stair-shaped profile for conductance indicates that several loads disconnected approximately 6 s after the FIDVR event was initiated and is due to thermal protection schemes tripping off residential A/C units. The reason why the waveform is a staircase and not smooth is that the number of A/Cs are around 10–15. If the conductance of a few thousand motors (corresponding to a load of tens of MW) are observed, the individual disconnections cannot be perceived, and the resulting conductance looks smooth as in Fig. 2.36.

Based on these observations and the admittance-based model, it is shown in [43, 44] that by measuring the admittance just after the FIDVR begins, the time durations t_1 and t_2 can be estimated from the load parameters and can be used as a way to quantify the severity of the FIDVR event. This will enable the localization of the FIDVR event both in offline simulations and in online stability monitoring from PMU measurements and will enable effective assessment of FIDVR.

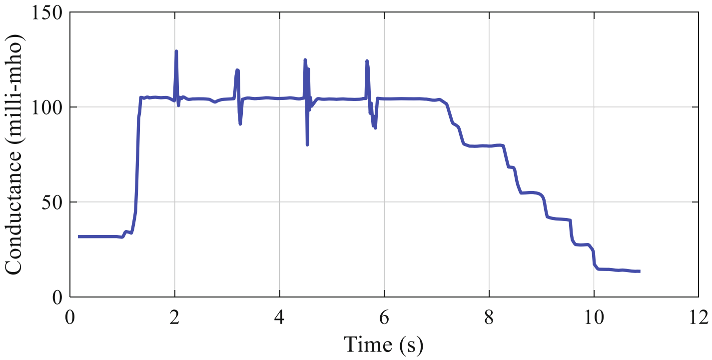

Fig. 2.37 Load conductance for the southern California FIDVR event on July 10, 2012 [43]

2.11 Effect of Distributed Energy Resources on Short-Term Voltage Stability

The significant increase in distributed energy resources (DERs)/distributed generation (DGs) is leading to the development of new performance and reliability standards. The Federal Energy Regulatory Commission (FERC) has recently announced [52] that DERs must ride through abnormal frequency and voltage events. It states that the specific ride through settings must be consistent with Good Utility Practice and any standards and guidelines applied by the transmission provider to other generating facilities on a comparable basis. It is also stated that they should have appropriate ride-through requirements comparable to large generating facilities.

The strong motivation behind these requirements is to ensure high reliability of the interconnected power system, and so, the DERs must continue to remain connected during disturbances and at the same time they cannot be connected indefinitely in the event of a fault or power system malfunction. The IEEE standard 1547 [53] provides the technical specifications for, and testing of, the interconnection and interoperability between utility electric power systems (EPSs) and DG sources. In this section, the focus is on the Voltage Ride Through (VRT) requirements pertaining to the IEEE standard 1547 as shown in Fig. 2.38.

Section R5 of the NERC standard TPL-001-4 [37] states that each transmission system planner shall have criteria for acceptable system voltage limits including voltage transients. Considering that the DGs can affect the transient voltages depending upon the ride-through capabilities, it is therefore imperative to examine

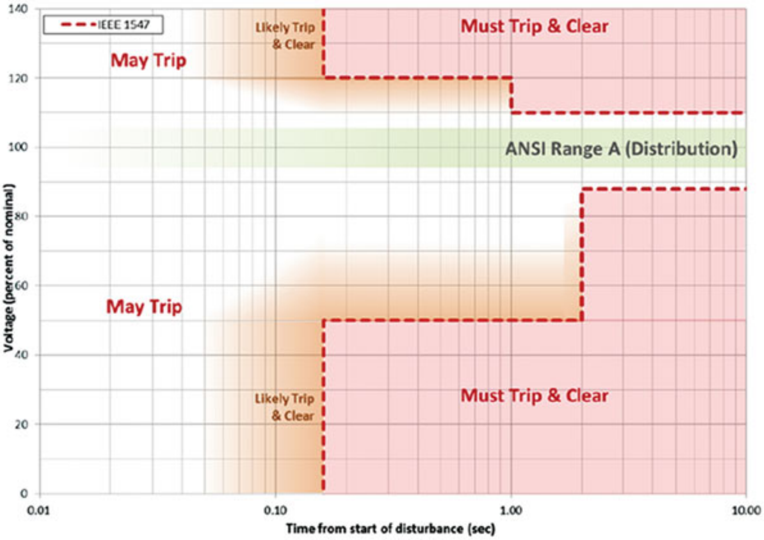

Fig. 2.38 IEEE standard 1547 voltage ride through requirement (extract from [53])

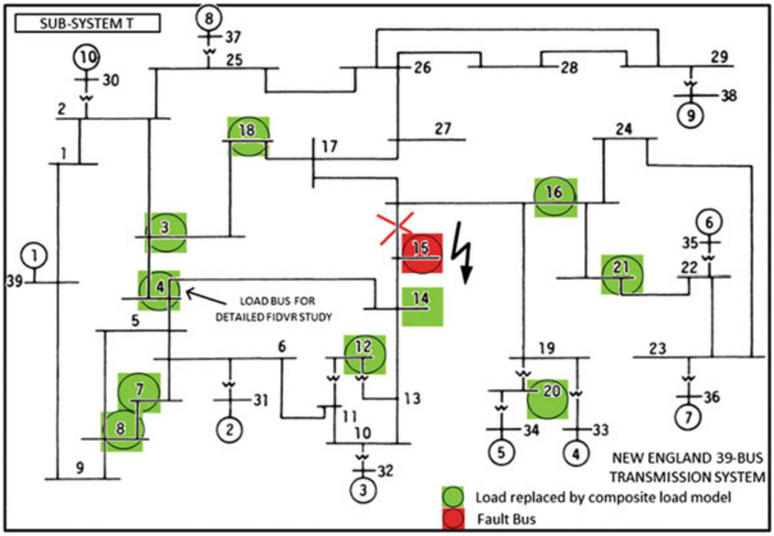

Fig. 2.39 New England 39-Bus transmission system with PQ load att 10 load buses replaced by equivalent composite load models with DG

the effect of the DG penetration on the power system dynamics. The DG present in the downstream feeders is lumped together into a single DG model that is modeled as a phasor representation of the DER inverter [54]. The power supplied by the DG is given by the fraction Fdg that specifies the DG power in terms of the power demanded by the load.

2.11.1 *Case Study with New England 39-Bus System*

The New England 39-bus system shown in Fig. 2.39 is considered for this study. This system has 29 load buses and 10 generator buses. The objective of this case study is to determine the effect of DGs on the delayed voltage recovery behavior. As this behavior is dependent on the voltage level at fault which determines the stalling characteristics of the induction motors located on that bus, we can selectively choose buses to replace the constant PQ load with the dynamic composite load model. Based on the voltage dip threshold criteria derived in [55], we identify those buses where the voltage goes below 0.75 pu due to a three-phase to ground fault applied at bus 15 followed by the removal of line 15–16 after a fault duration of 5 cycles, and replace the constant PQ load on these buses with the composite load model. The identified buses are 3, 4, 7, 8, 12, 14, 16, and 18. Buses 20 and 21 are also included due to their proximity to the fault. The fractions FmA, FmB, FmC, FmD, and Fel are all equal to 0.12 and the remaining power is in the static load. The fraction of

Table 2.4 DG VRT settings

Voltage range (% nominal)	Max clearing time (s)
<50%	0.16
50–88%	2.0
<110–120%	1.0
>120%	0.16

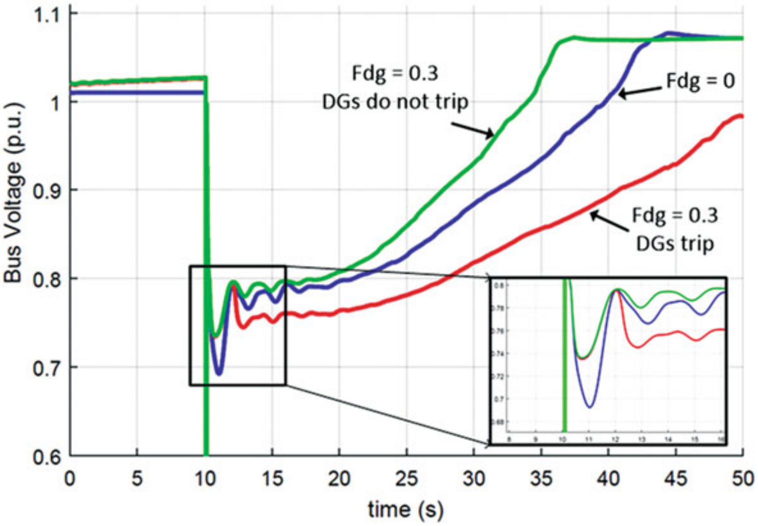

Fig. 2.40 Comparison of voltage recovery with DG tripping, not tripping against total absence of DG [54]

the DG (Fdg) for this case is 0.3. For the purpose of the study, the DG Voltage Ride Through (VRT) shown in Table 2.4 are applied.

In order to meet the Voltage Ride Through criteria, the DGs are modeled to meet the standards shown in Table 2.4. Figure 2.40 compares this case with (a) fault recovery in the absence of DG and (b) fault recovery in the presence of an always connected DG. From the plot, it can be ascertained that when DG exists, but then eventually trips, the recovery is much slower and can possibly cause a violation of the transient voltage criteria. This behavior is due to the fact that the DG, which was providing local active and reactive power, is suddenly disconnected, the voltage drops as a result of insufficient reactive and active power. In this case study, it is assumed that all the DGs will trip when their voltage levels are outside the no-trip boundary. According to IEEE standard 1547, the DGs cannot restart for 5 mins after tripping, provided that voltage and frequency have recovered to within tolerance. Therefore, in this case study, where the simulation is expected to run to approximately 1 min, the DGs are not set to restart after they trip.

2.12 Future Research Directions

As the key components that impact the short-term voltage stability of a system are induction motor loads and DERs with smart inverters that are physically present in the distribution system, representing the full distribution system dynamics instead of the aggregated composite load model has been of recent interest in utilities and in academia. As the traditional grid simulators for transmission and distribution systems have been developed and optimized over several years, applying a single tool to study the combined transmission and distribution dynamics often leads to numerical instabilities [54]. Instead, the recent literature has been focused on interfacing transmission and distribution system solvers and operating them in tandem by transferring common quantities at the boundary at each time step to perform co-simulation of Transmission-Distribution Systems. Capturing the dynamic behavior of the distribution system components is very important, an example is the August 2019 UK blackout that was driven by cascaded tripping of large number of smart inverters due to incorrect fault ride through settings in the smart inverters [56].

Academic researchers, Research Laboratories, and Industry are actively involved in the development of methods and tools using dynamic T&D co-simulation and data-driven methods for distribution system using micro-PMUs [54–56]. The industry and various utilities in association with various research laboratories are conducting research to further understand and explore the utilization of the distribution system assets to mitigate the short-term voltage instabilities by developing suitable control methods.

References

1. P. Kundur, J. Paserba, V. Ajjarapu, et al., Definition and classification of power system stability IEEE/CIGRE joint task force on stability terms and definitions. IEEE Trans. Power Syst. **19**(3), 1387–1401 (2004). https://doi.org/10.1109/TPWRS.2004.825981
2. N. Hatziargyriou, J.V. Milanovic, C. Rahmann, et al., “Definition and Classification of Power System Stability Revisited & Extended,” in IEEE Transactions on Power Systems, https://doi.org/10.1109/TPWRS.2020.3041774
3. N. Hatziargyriou, J. Milanovic, C. Rahmann, et al, “Stability definitions and characterization of dynamic behavior in systems with high penetration of power electronic interfaced technologies,” IEEE, Piscataway, NJ, USA, Tech. Rep. PES-TR77, 2020
4. P. Kundur, “Power System Stability and Control” textbook
5. P.W. Sauer, M.A. Pai, Power system steady-state stability and the load flow Jacobian. IEE Trans. Power Syst. **5**(4), 1374–1383 (1990)
6. V. Ajjarapu, *Computational Techniques for Voltage Stability Assessment and Control* (Springer Science Business Media, LLC, 2006)
7. S. Greene, I. Dobson, F.L. Alvarado, Sensitivity of the loading margin to voltage collapse with respect to arbitrary parameters. IEEE Trans. Power Syst. **12**(1), 262–272 (1997). https://doi.org/10.1109/59.574947
8. T.V. Cutsem, C. Vournas, *Voltage Stability of Electric Power Systems* (Text Book, Springer Science Business Media, LLC, 2008)

9. V. Vittal, Consequence and impact of electric utility industry restructuring on transient stability and small-signal stability analysis. Proc. IEEE **88**(2), 196–207 (2000). https://doi.org/10.1109/5.823998
10. “Distributed Energy Resources” NERC Report, Feb 2017. https://www.nerc.com/comm/Other/essntlrlbltysrvcstskfrcDL/Distributed_Energy_Resources_Report.pdf
11. Staff Report, “Distributed Energy Resources—Technical Considerations for the Bulk Power System”, Docket No. AD18–10-000, 2018
12. A.K. Bharati, V. Ajjarapu, Investigation of relevant distribution system representation with DG for voltage stability margin assessment. IEEE Trans. Power Syst. **35**(3), 2072–2081 (2020). https://doi.org/10.1109/TPWRS.2019.2950132
13. L.R. de Araujo, D.R.R. Penido, J.L.R. Pereira, S. Carneiro, Voltage security assessment on unbalanced multiphase distribution systems. IEEE Trans. Power Syst. **30**(6), 3201–3208 (2015). https://doi.org/10.1109/TPWRS.2014.2370098
14. X.-P. Zhang, J. Ping, E. Handschin, Continuation three-phase power flow: A tool for voltage stability analysis of unbalanced three-phase power systems. IEEE Trans. Power Syst. **20**(3), 1320–1329 (2005). https://doi.org/10.1109/TPWRS.2005.851950
15. H. Sun, Q. Guo, B. Zhang, Y. Guo, Z. Li, J. Wang, Master–slave-splitting based distributed global power flow method for integrated transmission and distribution analysis. IEEE Trans. Smart Grid **6**(3), 1484–1492 (2015)
16. Z. Li, *Distributed Transmission Distribution Coordinated Energy Management Based on Generalized Master-Slave Splitting Theory* (Springer Publications) Text Book
17. K. Vu, M.M. Begovic, D. Novosel, M.M. Saha, Use of local measurements to estimate voltage-stability margin. IEEE Trans. Power Syst. **14**(3), 1029–1035 (1999)
18. S. Corsi, G.N. Taranto, A real-time voltage instability identification algorithm based on local phasor measurements. IEEE Trans. Power Syst. **23**(3), 1271–1279 (2008)
19. F. Hu, K. Sun, A. Del Rosso, E. Farantatos, N. Bhatt, Measurement-based real-time voltage stability monitoring for load areas. IEEE Trans. Power Syst. **31**(4), 2787–2798 (2016)
20. M. Glavic, D. Novosel, E. Heredia, D. Kosterev, A. Salazar, F. Habibi-Ashrafi, M. Donnelly, See it fast to keep calm: Real-time voltage control under stressed conditions. IEEE Power Energy Mag. **10**(4), 43–55 (2012)
21. P. Kessel, H. Glavitsch, Estimating the voltage stability of a power system. IEEE Trans. Power Deliv.., PWRD- **1**, 346–354 (1986)
22. Y. Wang, I.R. Pordanjani, W. Li, W. Xu, T. Chen, E. Vaahedi, J. Gurney, Voltage stability monitoring based on the concept of coupled single-port circuit. IEEE Trans. Power Syst. **26**(4), 2154–2163 (2011)
23. H.Y. Su, C.W. Liu, Estimating the voltage stability margin using PMU measurements. IEEE Trans. Power Syst. **31**(4), 3221–3229 (2016)
24. L. Ramirez and I. Dobson, “Monitoring voltage collapse margin with synchrophasors across transmission corridors with multiple lines and multiple contingencies,” 2015 IEEE Power & Energy Society General Meeting, Denver, CO, 2015, pp. 1–5
25. S.S. Biswas and A.K. Srivastava, “Voltage Stability Monitoring in Power Systems, ” U.S. Patent, Feb. 25, 2014
26. A. Ramapuram-Matavalam, V. Ajjarapu, Sensitivity based Thevenin index with systematic inclusion of reactive power limits. IEEE Trans. Power Syst. **33**(1), 932–942 (2018)
27. C. Canizares, A. De Souza, V. Quintana, Comparison of performance indices for detection of proximity to voltage collapse. IEEE Trans. Power Syst. **11**(3), 1441–1450 (1996)
28. V. Ajjarapu, C. Christy, The continuation power flow: A tool for steady state voltage stability analysis. IEEE Trans. Power Syst. **7**(1), 416–423 (1992)
29. A.R. Ramapuram Matavalam, A. Singhal, V. Ajjarapu, Monitoring long term voltage instability due to distribution and transmission interaction using unbalanced μPMU and PMU measurements. IEEE Trans. Smart Grid **11**(1), 873–883 (2020). https://doi.org/10.1109/TSG.2019.2917676
30. A.R. Ramapuram Matavalam, A. Singhal and V. Ajjarapu, “Identifying Long Term Voltage Stability Caused by Distribution Systems vs Transmission Systems,” 2018 IEEE Power &

Energy Society General Meeting (PESGM), Portland, OR, 2018, pp. 1–5, doi: https://doi.org/10.1109/PESGM.2018.8586328
31. DOE-NERC FIDVR Conf., Sep. 29, 2009. [Online]. Available: http://www.nerc.com/files/FIDVR-Conference-Presentations-9-29-09.pdf
32. R.D. Quint, "A Look into Load Modeling: The Composite Load Model, Dynamic Load Modeling and FIDVR Workshop," https://esdr.lbl.gov/sites/all/files/6b-quint-composite-load-model-data.pdf, 2015
33. Consortium of Electric Reliability Technology Solutions, "Fault Induced Delayed Voltage Recovery (FIDVR), https://certs.lbl.gov/initiatives/fidvr
34. Modeling and Validation Work Group, "White paper on modeling and studying FIDVR events," Western Electricity Coordinating Council, Technical Report, October 20 (2011)
35. S. Robles, "2012 FIDVR Events Analysis on Valley Distribution Circuits," LBNL report by Southern California Edison, 2013
36. A. von Meier et al., Precision micro-Synchrophasors for distribution systems: A summary of applications. IEEE Trans. Smart Grid **8**, 6 (2017)
37. NERC, "Standard TPL-001-4—Transmission System Planning Performance Requirements," http://www.nerc.com/files/TPL-001-4.pdf, 2014
38. PJM Transmission Planning Department, "EXELON Transmission Planning Criteria", March 11, 2009
39. North American Transmission Forum, Transient voltage criteria reference document, 2016
40. WECC, "WECC Dynamic Composite Load Model Specifications," https://www.wecc.biz/Reliability/WECC%20Composite%20Load%20Model%20Specifications%2001-27-2015.docx, 2015
41. P.C. Krause, O. Wasynczuk, S.D. Sudhoff, P.C. Kraus, Analysis of electric machinery and drive systems. New York: IEEE Press. (2002)
42. Siemens PTI Power Technologies Inc., PSS/E 33, Program Application Guide, Vol. II, 2011
43. A.R. Ramapuram Matavalam, V. Ajjarapu, PMU-based monitoring and mitigation of delayed voltage recovery using admittances. IEEE Trans. Power Syst. **34**(6), 4451–4463 (2019)
44. A.R. Ramapuram Matavalam," Online monitoring & mitigation of voltage instability in transmission and distribution systems using synchrophasors", PhD Dissertation, Iowa State University
45. Load Model Data Tool [online] https://svn.pnl.gov/LoadTool
46. K. Zhang, H. Zhu, S. Guo, Dependency analysis and improved parameter estimation for dynamic composite load modeling. IEEE Trans. Power Syst. **32**(4), 3287–3297 (2017). https://doi.org/10.1109/TPWRS.2016.2623629
47. M.W. Tenza, and S. Ghiocel. "An analysis of the sensitivity of WECC grid planning models to assumptions regarding the composition of loads." Mitsubishi Electric Power Products (2016)
48. M. Paramasivam, "Dynamic optimization based reactive power planning for improving short-term voltage performance", PhD Dissertation, Iowa State University
49. S. Dasgupta, M. Paramasivam, U. Vaidya, V. Ajjarapu, Real-time monitoring of short-term voltage stability using PMU data. IEEE Trans. Power Syst. **28**(4), 3702–3711 (2013)
50. M.T. Rosenstein, J.J. Collins, C.J.D. Luca, D. Luca, A practical method for calculating largest Lyapunov exponents from small data sets. Physica D: Nonlin. Phenom. **65**(1–2), 117–134 (1993)
51. A. Reddy, K. Ekmen, V. Ajjarapu and U. Vaidya, "PMU based real-time short term voltage stability monitoring—Analysis and implementation on a real-time test bed," 2014 North American Power Symposium (NAPS), Pullman, WA, 2014, pp. 1–6
52. Federal Energy Regulatory Commission, "Requirements for Frequency and Voltage Ride Through Capability of Small Generating Facilities," https://www.ferc.gov/whats-new/comm-meet/2016/072116/E-11.pdf, 2016
53. IEEE Standard for Interconnection and Interoperability of Distributed Energy Resources with Associated Electric Power Systems Interfaces," in IEEE Std 1547–2018 (Revision of IEEE Std 1547–2003), vol., no., pp.1–138, 6 April 2018

54. R. Venkatraman, S.K. Khaitan, V. Ajjarapu, Dynamic co-simulation methods for combined transmission-distribution system with integration time step impact on convergence. IEEE Trans. Power Syst. **34**(2), 1171–1181 (2019)
55. Q. Huang, V. Vittal, Application of electromagnetic transient-transient stability hybrid simulation to FIDVR study. IEEE Trans. Power Syst. **31**(4), 2634–2646 (2016)
56. National Grid ESO, "Technical Report on the events of 9 August 2019", Report 6th September 2019
57. A.K. Bharati, V. Ajjarapu, "A Scalable Multi-Timescale T&D Co-Simulation Framework using HELICS", 2021 IEEE Texas Power and Energy Conference (TPEC), College Station, TX, USA, 2021.